

## Research Article

# Design and Performance Evaluation of Propeller for Solar-Powered High-Altitude Long-Endurance Unmanned Aerial Vehicle

Donghun Park<sup>1</sup>, Yunggyo Lee,<sup>2</sup> Taehwan Cho,<sup>2</sup> and Cheolwan Kim<sup>2</sup>

<sup>1</sup>Department of Aerospace Engineering, Pusan National University, Busan 46241, Republic of Korea

<sup>2</sup>Aerodynamics Research Team, Korea Aerospace Research Institute, Daejeon 34133, Republic of Korea

Correspondence should be addressed to Donghun Park; parkdh@pusan.ac.kr

Received 22 March 2018; Accepted 21 June 2018; Published 1 August 2018

Academic Editor: Mahmut Reyhanoglu

Copyright © 2018 Donghun Park et al. This is an open access article distributed under the Creative Commons Attribution License, which permits unrestricted use, distribution, and reproduction in any medium, provided the original work is properly cited.

Design, wind tunnel test, computational fluid dynamics (CFD) analysis, and flight test data analysis are conducted for the propeller of EAV-3, which is a solar-powered high-altitude long-endurance unmanned aerial vehicle developed by Korea Aerospace Research Institute. The blade element momentum theory, in conjunction with minimum induced loss, is used as a basic design method. Airfoil data are obtained from CFD analysis, which takes into account the low Reynolds number effect. The response surface is evaluated for design variables by using design of experiment and kriging metamodel. The optimization is based on desirability function. A wind tunnel test is conducted on the designed propeller. Numerical analyses are performed by using a commercial CFD code, and results are compared with those obtained from the design code and wind tunnel test data. Flight test data are analyzed based on several approximations and assumptions. The propeller performance is in good agreement with the numerical and measurement data in terms of tendency and behavior. The comparison of data confirms that the design method, wind tunnel test, and CFD analysis used in this study are practically useful and valid for the development of a high-altitude propeller.

## 1. Introduction

High-altitude long-endurance (HALE) unmanned aerial vehicles (UAVs) have gained considerable interest because their use could replace several of the functions of a satellite, such as earth observation, telecommunication, reconnaissance, and surveillance. HALE UAV has significant advantages over satellites in terms of low production cost, effective operation, and easy maintenance through landing/takeoff. In addition, as interest in green technology increases, a number of countries are actively researching and developing electric-powered or solar-powered HALE UAVs [1–4]. Among the well-known examples is Helios [5, 6], developed by NASA and the Aeronautical Environment Corporation (UAS). In 2003, it ascended to an altitude of over 29 km, the highest climb record in the world achieved by a propeller-driven UAV at that time. Another successful and widely known example is Zephyr [7, 8], which was designed and built by

the British company, QinetiQ. It holds the official endurance world record. It is currently being developed as a part of the Airbus high-altitude pseudosatellite (HAPS) program. In recent years, large IT companies have given considerable attention to HALE UAVs for the purpose of internet distribution. For example, Google acquired Titan Aerospace and is developing Solara 50 and 60, whereas Facebook is developing Aquila. Other examples include the Solar Eagle, which was developed by Boeing (DARPA Vulture II Program) [9].

Recently, the Korea Aerospace Research Institute (KARI) built a series of solar-powered HALE UAVs through a research program. In this program, KARI is aimed at exploring, developing, and demonstrating the underlying technologies needed for the development of an electric-powered HALE UAV. The scale-down version, EAV-2H+, was developed and flight tested during which it ascended up to an altitude of 10 km [10, 11]. Thereafter, KARI developed the full-scale version, EAV-3, which successfully soared above

18 km during its test flight [12–14]. The flight of the EAV-3 is third in the world record for an electric-powered UAV to ascend at an altitude of over 18 km.

In developing HALE UAV, state-of-art technologies in all fields, including aerodynamics and structural design, composite materials, solar cells and rechargeable battery (energy system), electric-motors, propellers, flight stability and control, and system integration, must be incorporated. From the perspective of aerodynamics, its performance could be significantly degraded due to low Reynolds number flows formed by the low air density at altitudes of over 10 km. To improve performances such as the lift-to-drag ratio and drag characteristics, the sizing and aerodynamic configuration design must be carefully conducted, taking into consideration the low Reynolds number environment. Additionally, since an electric-powered HALE UAV uses propellers for propulsion, the high efficiency of these propellers is essential for the endurance and climb capability of HALE. However, at high altitudes, propellers are vulnerable to efficiency reduction due to low Reynolds number conditions. Moreover, a design solely focused on maximizing the cruising efficiency at high altitudes may result in the considerable degradation of the performance at low altitudes or during climb operations.

Therefore, the proper design of propeller, considering various operating conditions and system constraints, is extremely important to achieve both climbing performance and endurance. Moreover, the accurate prediction and analysis of the propeller performance enables the establishment of a reliable and efficient mission profile. Thus, the design and performance prediction of the propeller are among the key technologies required for HALE UAV development.

Concepts on design, analysis, and testing of propellers for conventional aircrafts and UAVs have been well established through enormous research efforts expended for approximately a century. Although several solar-powered HALE UAVs have been designed and built, only a few literature pertain to design and performance evaluation of their propellers [15, 16]. As mentioned by Monk [15], the history of propellers is still sparse in the area of high-altitude applications. He reported and summarized findings from efforts in conjunction with the NASA ERAST program. The efforts include investigations into the existing propellers designed for height altitude flight condition, the analysis capability to performance estimation for a given design, and the acquisition of the performance data through experimental testing. Several examples of propeller-driven high-altitude aircrafts, design approaches and limitations, analysis approaches, and wind tunnel testing for 2D airfoil and 3D propellers are introduced. More recently, Monk [16] evaluated a propeller design based on minimum induced loss concept and analysis for performance prediction based on momentum theory for a HALE flight vehicle. A conceptual propeller was designed, and analyses were carried out for altitudes up to 15 km. The results from a wind tunnel testing for a scaled model showed reasonable agreement with the prediction.

In particular, literature that contain detailed information and data on propellers mounted on an actual HALE UAV are rather rare. With the EAV program, KARI acquired and demonstrated the fundamental technologies related to

propellers for solar-powered HALE UAVs and evaluated their reliability and feasibility. In this study, the design and performance evaluation of propellers, conducted during the development of EAV-3, are presented. The performance analysis includes CFD analysis, wind tunnel test, and flight test data analysis.

In Section 2, the design methodology and procedure for the EAV-3 propeller are introduced. The wind tunnel test and CFD analysis results are presented in Sections 3 and 4, respectively. A simple analysis of the flight test data to evaluate the propeller performance is given in Section 5. Finally, conclusion follows in Section 6.

## 2. Design of Propeller

Propellers for HALE UAVs operate under various operating conditions, ranging from the sea level to stratosphere altitudes. Apparently, it is appropriate to adopt a variable pitch system to provide the optimal propulsive efficiency under the aforementioned conditions. However, its adoption imposes additional weight and complexity due to the addition of actuators and pitch links. Additionally, these pitch links and actuators will practically be exposed to external flows at low temperatures from  $-70$  to  $-80^{\circ}\text{C}$  at stratospheric altitudes. The extreme environment and mechanical complexity may lead to an increased possibility of malfunctions and uncertainty. Consequently, the demand for reliability and being ultra-lightweight, which are top-level constraints of HALE UAVs, makes it difficult to adopt the variable pitch system. Therefore, fixed-pitch propellers are generally used. When the fixed-pitch propellers are optimized for aerodynamic performance at high-altitude operation, the required torque, approximately at sea level, becomes considerably large and exceeds the specification for electric motors. This can lead to low climbing performances or, sometimes, the inability to climb. On the other hand, as altitude increases, the rotational speed of the propeller gradually increments, which consequently results in an increase of the required power. Thus, the maximum required power occurs under high-altitude climbing conditions. In this respect, the design of HALE UAV propellers must not only take into account the two conflicting constraints but also simultaneously maximize efficiency under the desired operating condition.

*2.1. Design Requirement and Constraints.* The ultra-lightweight aircraft, EAV-3, has a wingspan, total length, and design total weight of approximately 19.5 m, 8.9 m, and 46.5 kg, respectively. It uses twin propellers mounted on each wing. The specifications, configuration, geometry, and mission profile of EAV-3 can be found in literature [14]. The operating conditions and required thrust for each propeller are summarized in Table 1. The specifications of the direct current (DC) motor, which is developed and customized for EAV-3, are listed in Table 2. The maximum available torque should correspond to the climb condition at sea level, requiring the highest thrust. The maximum power condition should correspond to the climb operation at 18 km, where the highest rotational speed is required. Considering the motor diameter, the design spinner diameter was fixed at 0.16 m

TABLE 1: Design operating condition and required thrust for each propeller.

Altitude	Speed (m/s)	Thrust (N)
Sea level	5.8	38.8
10 km	10.0	26.6
15 km	14.6	21.3
18 km	18.5	18.8

TABLE 2: Specification of DC motor.

Power (W)	RPM	Torque (Nm)	Note
314	1200	2.5	Rated condition
351	880	3.8	Maximum torque
369	2200	1.6	Maximum power

as a geometry constraint. In conformance with the EAV-3 mission profile, which is mainly aimed at climbing to high altitudes, the climb condition of 15 km was set as the propeller design point.

**2.2. Basic Design Methodology.** The blade element momentum theory (BEMT) [17] is a useful basic methodology for propeller design and analysis. It is the most common engineering model and still widely used due to its simplicity and easy applicability with various corrections and modifications [18–21]. There are several free software that use BEMT for propeller design and analysis. For example, JBLADE [22] or JavaProp [23] are easy to get online. However, these cannot be modified by the user, airfoil selection is limited to a given list, and airfoil aerodynamic data in the low Reynolds number range are less reliable. Consequently, a BEMT-based design and analysis code was independently developed and utilized for EAV-3 propellers. This code allowed the easy modification of details and use of any airfoil by supplying customized aerodynamic data. The code was based on the theory of Adkins and Liebeck using BEMT and minimum energy loss condition [24]. To take into account the tip loss effect, the tip loss corrections of Glauert [17] were implemented. A graphical user interface was constructed so as to enhance the user convenience in the early design stage and off-design analysis. The concept and input/output of the code are shown in Figure 1. Further details on the design code can be found in [25].

Operating conditions such as forward flight velocity, rotational speed (rpm), and air properties (density) at design point are essential input parameters. The input parameters for the geometry are the diameter, spinner diameter, and section airfoil. The distribution of the section lift coefficient along the blade span also needs to be prescribed. The design can be conducted when the foregoing input parameters and target performance are given. The target performance can be the desired thrust, torque, or power. The results of the design yield blade geometry information, specifically the distribution of the sectional chord and twist angle.

**2.3. Blade Airfoil and Airfoil Data.** Airfoil aerodynamic data are essential for BEMT calculations and are key factors in determining the accuracy of design and performance prediction. Since blade elements operate at various Reynolds numbers and angle of attacks, it is efficient to construct the set of aerodynamic data in advance. The required lift and drag coefficient at a specific condition of interest can be simply and quickly obtained through table look-up or interpolation of the data.

In general, fast analysis tools such as XFOIL [26] and XFLR5 [27] are reasonable options for obtaining airfoil data due to their low computational costs. XFOIL is the most widely used tool in previous studies [19–21]. However, in the case of EAV-3 propellers, blade elements will be placed under conditions where the Reynolds number is less than  $10^5$ . The authors of the present study attempted to evaluate the reliability of airfoil data under these low Re conditions prior to the use of fast analysis tools.

Figure 2 shows result examples of the airfoil analysis by using XFOIL and CFD. The airfoil is DAE51, and the Reynolds number and angle of attack are  $10^5$  and  $0^\circ$ , respectively (chord length 0.2 m). A two-dimensional, C–H-type structured grid with quadrilateral cells is used. The total number of cells is 165600, and 300 grid points are used along each upper and lower surfaces. The height of the first cell from the surface is set as  $y^+$  which remains below 1 over most of the airfoil surface. The computational domain extends to 30 chord to upstream, top, and bottom directions and 60 chord to downstream direction. CFD analyses were carried out by using Fluent 17.0 [28] and for the two cases of  $k$ - $\omega$  SST and  $\gamma$ - $Re_\theta$  [29] based (four-equation) transition-SST turbulence models. The inlet turbulence intensity is set to 0.1%. The distributions of pressure and skin friction coefficients on both upper and lower surfaces are compared in the figure.

From previous studies [30–33], it is well known that the characteristics of flow around an airfoil at low Reynolds numbers are considerably different from those at moderate and high Reynolds numbers. The separation of the laminar boundary layer and transition in the separated flow region followed by a reattachment form a separation bubble on the airfoil surface. A typical feature of low Reynolds number flow is the formation of a large separation bubble at low angle of attacks. Moreover, the streamwise extent and position of the bubble dynamically change with the angle of attack.

As can be observed in Figure 2, a typical characteristic at low Reynolds number flow is represented by a practically flat region in the pressure coefficient distribution followed by an abrupt break, which corresponds to the existence of the separation bubble. However, it can be seen from the figure that the result of the  $k$ - $\omega$  SST model does not show this feature, which indicates that this model cannot capture the flow feature and bubble properly. Additionally, the friction coefficient values are large, which correspond to a fully turbulent boundary layer and results in a high viscous drag. Since the  $k$ - $\omega$  SST model assumes a fully turbulent flow, it cannot accurately reflect the actual phenomena occurring under low Reynolds number conditions. On the other hand, results from the transition SST model and XFOIL show practically similar distributions of surface pressure and skin friction. It

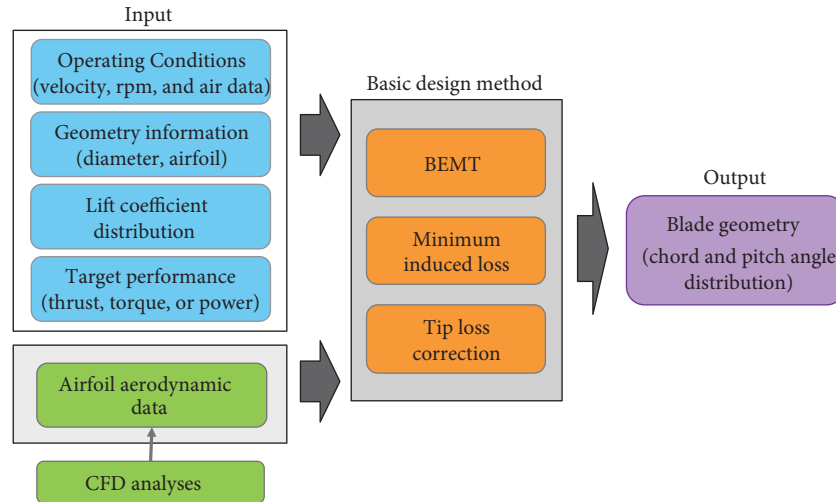


FIGURE 1: Schematic of the basic propeller design code.

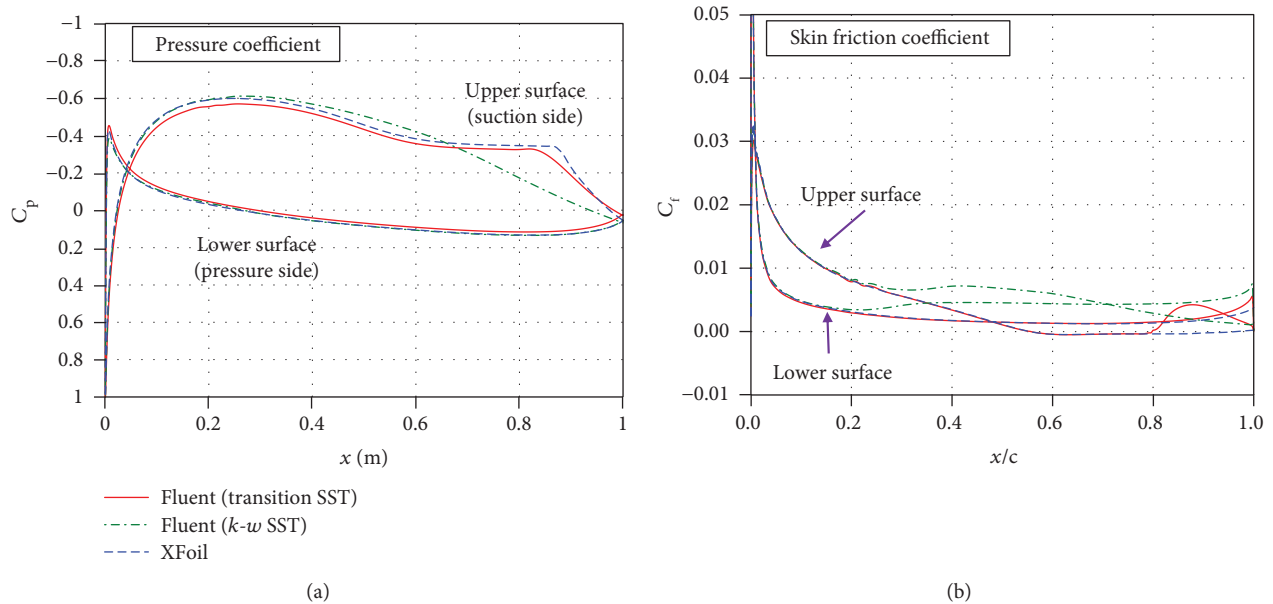


FIGURE 2: Comparison of XFOIL and CFD results for an airfoil at low Reynolds number.

can be deduced that essential elements, such as the laminar boundary layer separation, transition, and reattachment, are properly captured in those two calculations. However, XFOIL results exhibit notable differences in the predicted friction at the turbulent boundary layer region after the reattachment.

The differences of aerodynamic coefficients are shown in Figure 3, which compare the drag polar calculated by three methods. The results of the  $k-\omega$  SST model corresponds to a typical parabolic drag polar at high Reynolds numbers and are not suitable for the calculation of airfoil data at low Reynolds number regions. Although two results of the transition SST model and the XFOIL show the typical drag polar at low Reynolds numbers, their difference in drag increases as the angle of attack increases. The same calculations were

conducted for several different Reynolds numbers. From the results, low Reynolds number characteristics began to distinctly appear as the Reynolds number becomes lower as  $2 \times 10^5$ . It was confirmed that the aerodynamic coefficient and drag polar considerably change with respect to the Reynolds number in the region around  $10^5$  and below. Moreover, the difference between the results of the transition SST model and XFOIL was found to increase gradually as the Reynolds number decreased. From the comparison with available wind tunnel testing data [30, 31] and previous numerical study [34], it was deduced that the CFD result with the transition SST model was more reliable than that of XFOIL for the friction in the turbulent boundary layer after reattachment. Accordingly, it was decided to use CFD to calculate and construct airfoil data for the EAV-3 propeller design.

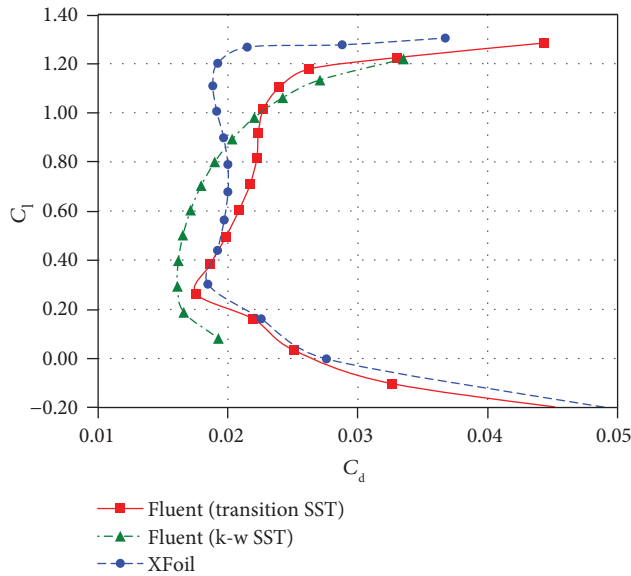


FIGURE 3: Comparison of drag polar calculated by three methods.

Analyses of several candidate airfoils used in low Reynolds numbers were performed, and aerodynamic characteristics were compared within the operating range of the angle of attack near the design point. At Reynolds numbers of  $3.0 \times 10^5$  or less, SG6043 and DAE51 were considered to be superior airfoils in terms of the lift-to-drag ratio. However, DAE51 and E387 exhibited rather higher performance at Reynolds numbers below  $1.5 \times 10^5$ . From preliminary studies, we expect that the most of section Reynolds number is lower than  $1.0 \times 10^5$  at design point. As an example, Figure 4 shows CFD results for several airfoils at Reynolds number of  $1.0 \times 10^5$ . All calculations were conducted by using the transition SST model. We readily see that DAE51 shows a good lift-to-drag ratio over a wide range of angle of attack for the linear region. Although E387 also exhibits a good lift-to-drag ratio, it is limited to only an angle attack range for lift coefficients less than 0.8 and has a rather lower lift slope and the maximum lift coefficient. Similar comparison and examination were made for the other Reynolds numbers. By taking into account the desired lift coefficient which is between 0.6 and 1.0 for low Reynolds number operation, we concluded that DAE51 is a reasonable choice for the propeller blade airfoil.

Airfoil data of DAE51 as an input for a propeller design code was obtained by using CFD with the transition SST model. The incompressible and unsteady (pressure-based and transient in Fluent, resp.) calculations were conducted using a second-order scheme for both time and spatial discretization. The calculations for Reynolds numbers ranging from  $10^4$  to  $10^5$  were carried out at intervals of  $10^4$ . Calculations for Reynolds numbers at 1.5, 2.0, 3.0, 4.0, and  $5.0 \times 10^5$  were also conducted. For each Reynolds number, angle of attacks, from  $-10$  to  $20^\circ$ , at intervals of  $1^\circ$ , were considered.

Figure 5 shows an example of DAE51 airfoil data calculated for several Reynolds number conditions. Aerodynamic data beyond the range of computation were extended

following the method given in [35]. The correction for compressibility is applied using formulae described in [36]. However, it has little influence in our design because the Mach number is not sufficiently high to have a compressibility effect over the entire operating condition range.

**2.4. Design Variables and Effect of Lift Coefficients.** Along with the design code and airfoil data described above, design variables were identified and defined for the operating condition at design point. The diameter ( $d$ ) and rpm of the propeller are essential design variables. The remaining information that needs to be specified is the lift coefficient distribution along the blade span.

In traditional aircraft propeller design, a lift coefficient of 1.0 or greater is generally used to procure sufficient lift-to-drag ratio, which guarantees good aerodynamic efficiency of blade elements. However, as previously discussed, the lift coefficient and lift-to-drag ratio considerably deteriorate at high altitudes, where the Reynolds number is  $10^5$  or less (see Figure 5). When high lift coefficients are imposed even under this condition, there is a possibility that the lift coefficient cannot reach the given value as a design result. Otherwise, it can yield the design of lower efficiency originated from the low lift-to-drag ratio of the blade elements due to derivation of short chord length.

To avoid the foregoing possibility, the lift coefficient must be specified at lower values of certain degree than those in the traditional approach. Thus, for design, we assumed a lift coefficient distribution as a parabolic profile with its minimum value at a certain location in the spanwise direction along the blade. Recall that most of conventional design approaches use a constant lift coefficient along the span. The lift coefficient values at three different spanwise locations define a particular parabolic profile. In the present study, the lift coefficient at the location of the spinner was fixed at 1.0, taking into consideration the geometrical and structural constraints. The remaining two locations were chosen as 60% of radius ( $r/R=0.6$ ) and at the blade tip ( $r/R=1.0$ ). We note here that all parabolic profiles can be defined by specifying proper lift coefficient values at any three spanwise locations. The choice of  $r/R=0.6$  seems arbitrary; however, variation of the lift coefficient at this location can consider all the possible parabolic profiles for given values at the spinner and tip. A parabolic profile with a certain lift coefficient value at  $r/R=0.6$  would be identical to the profile with a different lift coefficient at some other spanwise location. Therefore, changing the lift coefficients at  $r/R=0.6$  and 1.0 is sufficient to explore all parabolic profiles of a fixed value at the spinner. Consequently, the lift coefficients at  $r/R=0.6$  and at the blade tip ( $r/R=1.0$ ) were chosen as additional design variables,  $cl_m$  and  $cl_t$ , respectively. The four design variables used in this study are listed in Table 3.

Example cases with several parabolic lift coefficient distributions were studied to evaluate the influence of the lift coefficient distribution on design results. The designs were conducted under the condition of design point with a fixed diameter and rpm and required thrust. Table 4 summarizes the values of  $cl_m$  and  $cl_t$  for five cases, and Figure 6(a)

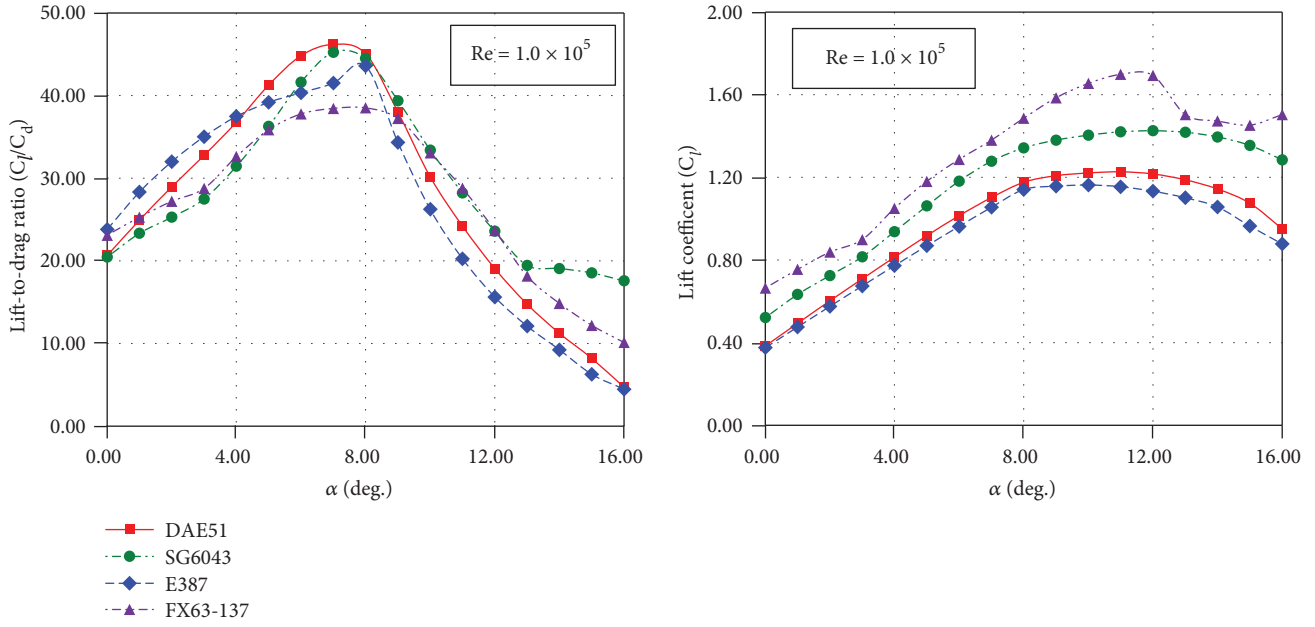


FIGURE 4: Example of CFD results for several airfoils at  $Re = 10^5$ .

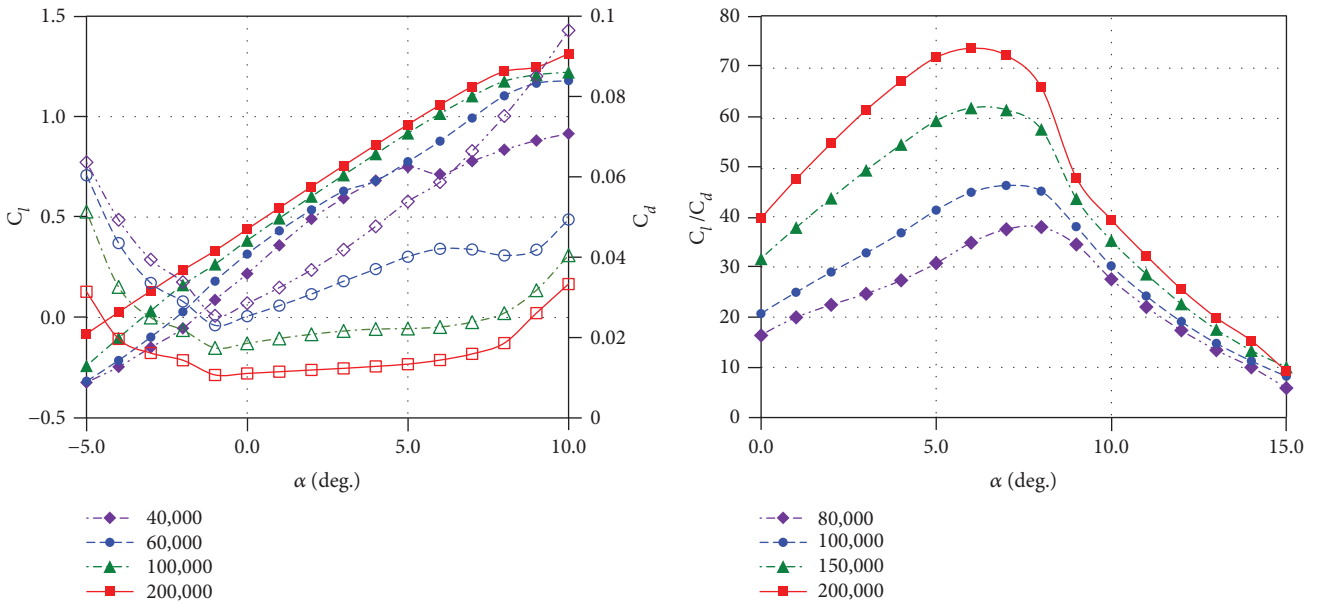


FIGURE 5: Example of aerodynamic data of DAE51 obtained by CFD.

TABLE 3: Design variables.

Symbol	Description
$d$	Propeller diameter
rpm	Rotational speed at design condition (rev./min)
clm	Lift coefficient at $r/R = 0.6$
clt	Lift coefficient at the blade tip

TABLE 4: Values of design variables for example cases.

Case	clm	clt
A	0.50	0.55
B	0.55	0.60
C	0.60	0.65
D	0.70	0.75
E	0.80	0.85

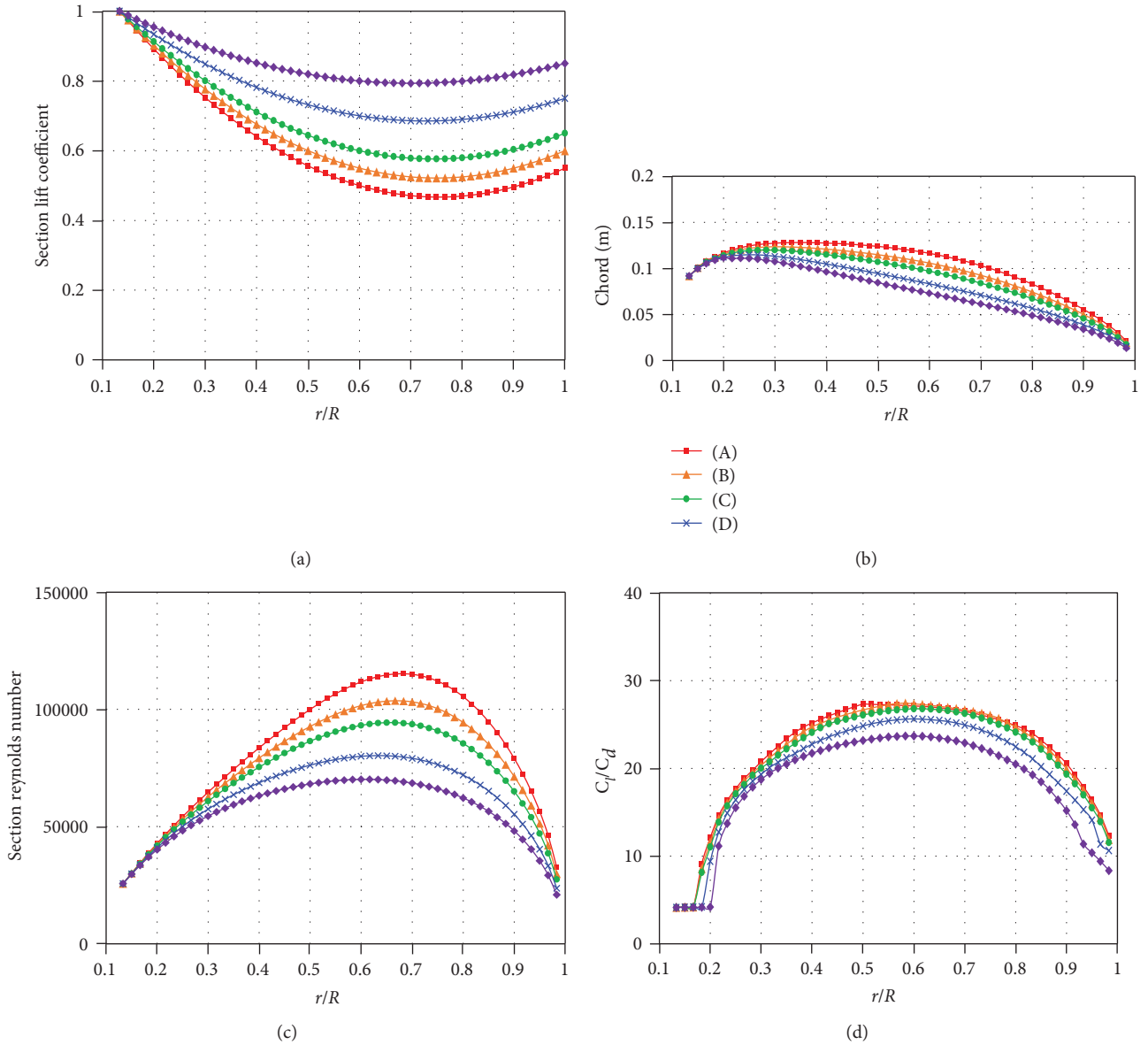


FIGURE 6: Effect of lift coefficient distribution on design.

shows the corresponding lift coefficient distributions. It is observed from Figure 6(b) that the design using the lower lift coefficient distribution yields a large chord length to produce the same thrust, which leads to a blade geometry with a relatively large planform area. It can be confirmed from Figures 6(c) and 6(d) that the higher chord Reynolds number yields a higher lift-to-drag ratio, which directly results to a higher efficiency of the propeller. It can be easily deduced that the chord length below a certain level can deteriorate the performance at high altitudes due to low chord Reynolds numbers. This means that a chord length greater than that at a certain level should be secured in order to improve efficiency. It is consistent with the observation that previous HALE UAVs have propeller blades with large chord length (large planform area) than conventional aircraft propellers. The same observations and discussions were made by Monk [16].

It was confirmed that it is possible to improve the efficiency of the propeller by imposing low values of the lift coefficient distribution. However, it should be that the benefits derived from the use of lower lift coefficients discussed above are limited up to a certain level of chord the Reynolds number only. The degree of improvement in the lift-to-drag ratio is gradually decreased as the Reynolds number increases (see Figure 6(d)). An excessively low lift coefficient will yield a large chord length that requires a high torque exceeding the limitation of the electric motor at low-altitude conditions. Therefore, it is necessary to carefully evaluate whether the flow is within the sufficiently low Reynolds number range at the design point, and whether imposing low lift coefficients will definitely improve performance.

*2.5. Response Surface Based on Kriging Metamodel.* For a given combination of design variables, the propeller design

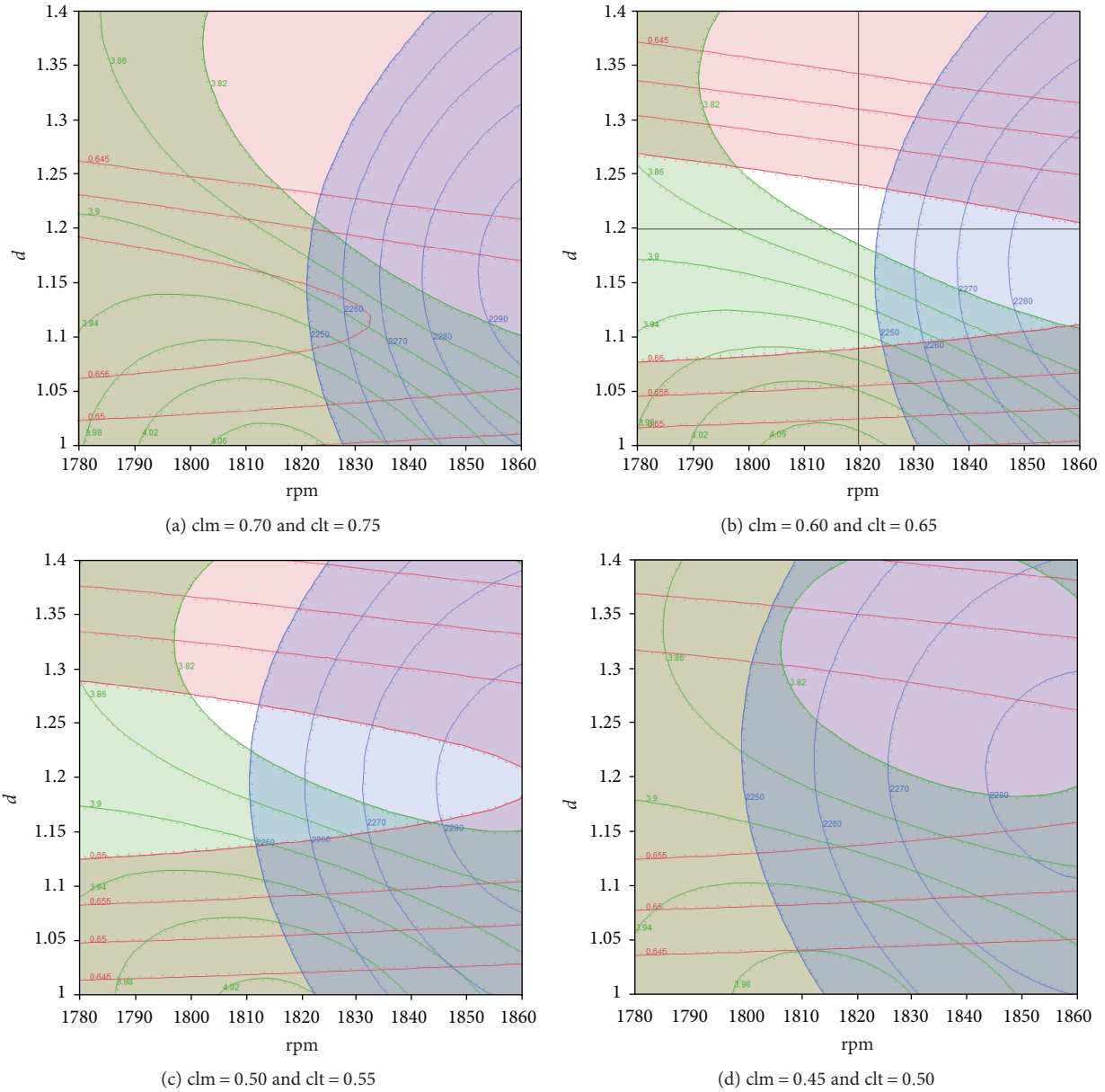


FIGURE 7: Contours of response surface from kriging metamodel (rpm- $d$  plane).

is uniquely determined by the methods described above. The efficiency of the propeller at the design point, required torque at sea level, and required rpm at altitude of 18 km were set as responses for each design. All three responses are evaluated for the climb condition at rate of climb of 1 m/s.

The parameter space of design variables was examined through a response surface methodology (RSM) [37]. Test points were generated through the design of experiment (DOE) [37], and the Latin hypercube sampling [38] is used as DOE method. The propeller design is conducted, and responses are calculated by off-design analysis for each test point. Using the responses, the kriging metamodel [39] was generated to construct the response surface for each response. The DOE and Gaussian process for the metamodel generation were carried out using the commercial program JMP 9.0 [40].

Thirty-two design variable combinations (test points) were extracted by using DOE of Latin hypercube option implemented in JMP. Using the propeller design and analysis code, a propeller for each combination was designed and efficiency at the design point was obtained. For each propeller, the required torque at sea level and rpm at 18.5 km are computed from off-design analysis. Then, the data of three responses for all propellers are mounted to JMP for generation of the kriging metamodel. Since design and off-design analyses are needed only for 32 propeller cases, the interaction of JMP 9.0 with the other tools was not automated. The design, off-design analysis, data recording, synthesis, and transfer were carried out manually.

Figure 7 shows the response surface contours of three responses on an rpm- $d$  plane for several cases of lift coefficient distributions. In each figure, the abscissa is rpm,

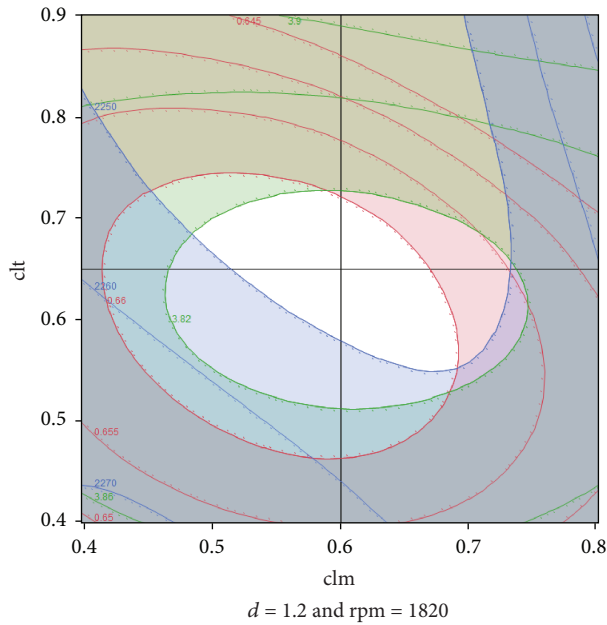


FIGURE 8: Example contour of response surface from the kriging metamodel (clm-clt plane).

centered at 1820 with an interval of 10, whereas the ordinate is  $d$ , centered at 1.2 m with an interval of 0.05 m. Each shaded area represents the combination of design variables, corresponding to an unallowable design due to a constraint on any one of the three responses. The area shaded in red corresponds to designs in which the efficiency is less than 66% at the design point. The green shaded area represents designs in which the required torque exceeds 3.82 N·m at sea level. Similarly, the blue shaded area shows the designs in which rpm at an altitude of 18 km exceeds 2250. The available designs which satisfy all the constraints with efficiency greater than 66% are designs corresponding to the unshaded area only. It is observed from Figure 7 that only a limited range of design variables yields an allowable design. There is no possible design for the lift coefficient distribution greater than 0.7 (Figure 7(a)). It was confirmed that only clm and clt values, approximately between 0.5 and 0.7, allow possible designs with limited combination of diameter and rpm (see Figures 7(b) and 7(c)). Moreover, there are no available designs for values less than 0.5 (see Figure 7(d)). Changing the diameter and rpm in the direction of the maximum efficiency at the design point is bounded by constraints of the required motor performance at sea level and altitude of 18.5 km.

Figure 8 shows another response surface contour on the clm-clt plane for  $d = 1.2$  m and  $\text{rpm} = 1820$ . We see again that only limited ranges of clm and clt give allowable design for a given diameter and rpm. Similarly, we examined response surfaces for several diameters and rpms. The diameter and rpm with an interval of 0.01 m and 20, respectively, were considered. It was confirmed that available designs exist only for diameters within 1.17–1.29 m. For an rpm lower than 1820, although a higher efficiency design can be possible due to increased chord length, the required torque at sea level exceeds the maximum torque of the motor. On the other

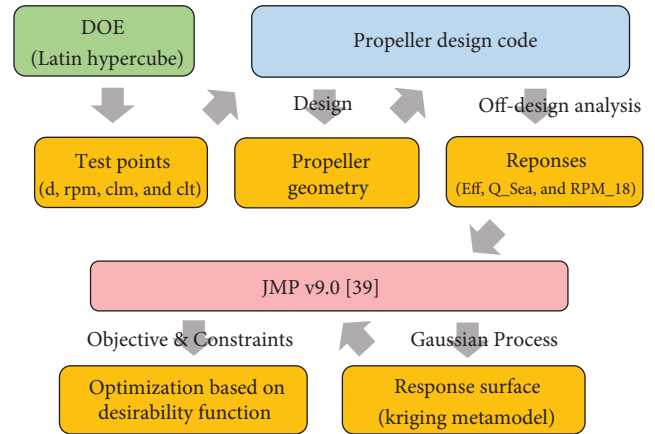


FIGURE 9: Schematic of optimization process.

hand, for an rpm higher than 1820, although the maximum torque constraint is satisfied, the efficiency is decreased due to the shortened chord length, and the rpm at an altitude of 18 km exceeded the motor specification.

**2.6. Optimization Based on Desirability Function.** The optimization was conducted based on the concept of the desirability function by using JMP. Figure 9 depicts the basic procedure for the optimization. The objective functions, constraint functions, and response surfaces for responses must be defined prior to exploring an optimal solution based on desirability. The objective function was set to maximize the propeller efficiency at the design point. Two constraint functions were defined for the required torque at the sea level and required rpm at an altitude of 18 km. Considering motor specifications, the torque and rpm constraints were set so as not to exceed 3.82 Nm and 2250, respectively. The kriging metamodel described in the previous subsection is used as response surfaces.

The desirability functions must be set to achieve the objective and constraints for each response surface. The desirability was set in the direction of maximizing the efficiency and minimizing the torque and rpm. In addition, the weight for each desirability function needs to be imposed according to importance. The importance was set to 1.0, 0.8, and 0.6 for efficiency, torque, and rpm, respectively. For the desirability function and weights provided, we explored and determined the optimal solution. Figure 10 shows the determination of optimal solution conducted by using JMP. The optimal solution was found as 1.22, 1817.9, 0.482, and 0.648 for  $d$ , rpm, clm, and clt, respectively. It was observed that the optimal solution can be slightly changed by the imposed values on importance. The solutions corresponding to various imposed values on importance for the torque and rpm constraints were obtained and examined. Since the maximizing efficiency at the design point is the main objective of the present design, importance for efficiency was fixed to 1.0. The results indicated that the influence of changing importance between 0.4 and 1.0 does not noticeable in the solution within 3 digits.

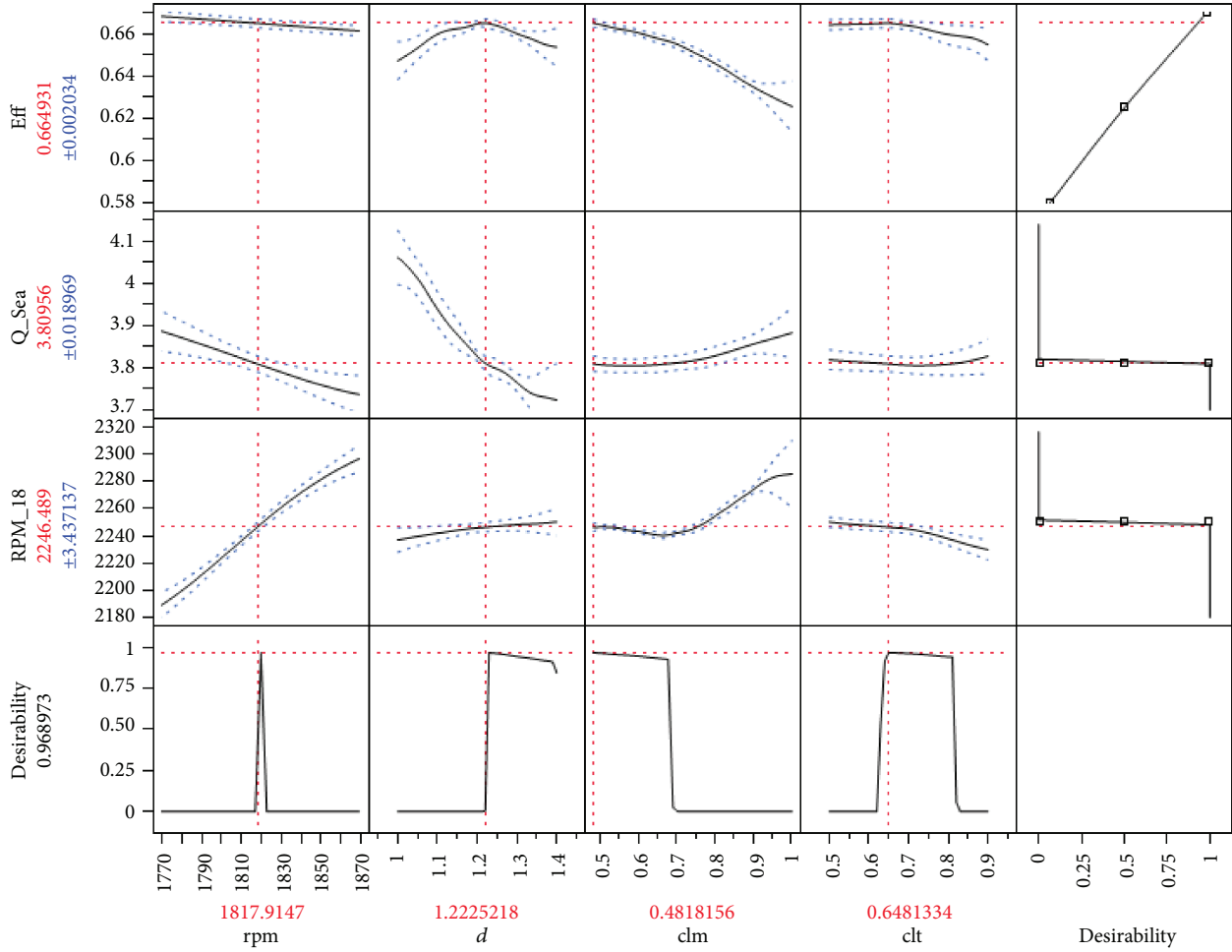


FIGURE 10: Optimization based on desirability function in JMP.

TABLE 5: Comparison of optimization and final adjusted design of the EAV-3 propeller.

Case	$d$	rpm	clm	clt	Efficiency
Optimization	1.22	1817.9	0.482	0.648	0.6633
Final design (adjust)	1.2	1820	0.60	0.65	0.6604

2.7. Final Design and Manufacturing. The result of the optimization described in the previous subsection is summarized in Table 5. The optimized result was examined, and the design was slightly adjusted by considering manufacturing, system integration, and requirements from other disciplines and so on. The diameter and rpm were truncated to 1.2 m and 1820, respectively, which are the nearest value from the optimization. We reviewed the response surface for  $d = 1.2$  m and rotation speed at 1820 rpm, which is already shown in Figure 8. The optimized value of clm (0.482) is located around the left boundary of the region for allowable design, and approximately lies at the boundary defined by rpm constraint at 18 km. Since the development of a customized motor was under progress at that time, it was decided to impose a margin on the propeller design considering the

uncertainty of motor specification. The clm value was adjusted to a higher value of 0.60 to relieve the motor requirement. The value is approximately at the center of the region of available design, which is marked as a vertical solid line (see Figure 8). The clt value is truncated to 0.65, which is marked as a horizontal solid line in the figure. These adjustments are compromised by the efficiency reduction of 0.29%p at the design point, as given in Table 5.

Figure 11 illustrates the comparison of chord (planform geometry) and twist angle distributions between the optimization and final adjusted design. It can be seen from Figure 11 that adjusted design has a slightly short chord length at the midspan region. This is primarily due to the adjustment of clm to a higher value. This behavior is discussed in Section 2.4. In the adjusted design, the twist angle at the midspan region is slightly increased to compensate for the decrease in chord length (see Figure 11(b)). Furthermore, in order to achieve sufficient structural robustness, the structural design, analysis, and static load test were independently conducted. To avoid structural interference by the motor and achieve short length of rotational axis, the design twist angle was adjusted by limiting it to  $50^\circ$  in the transition region at spinner location ( $r = 0.08-0.12$  m,

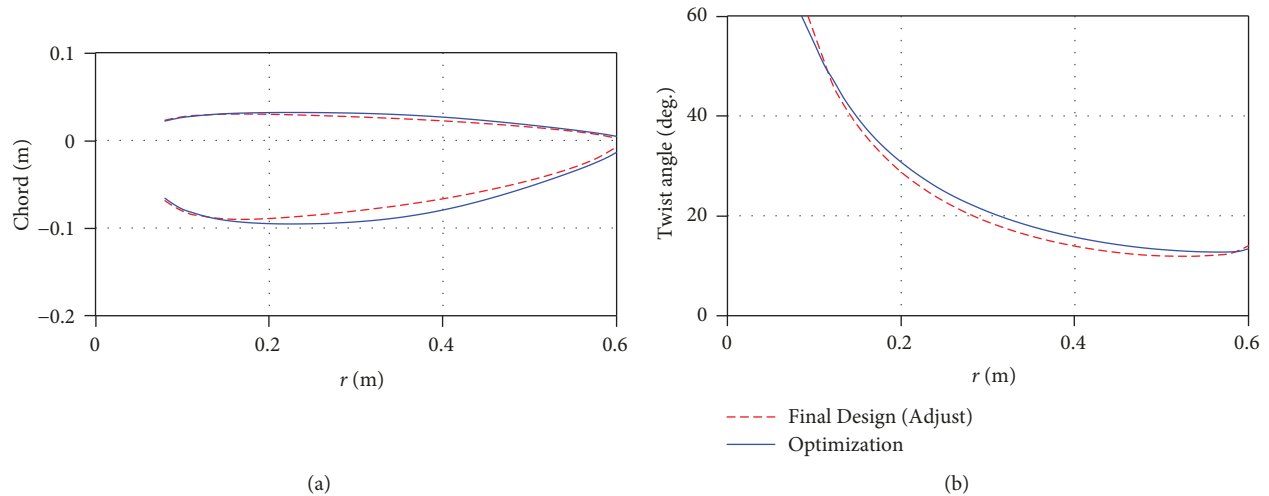


FIGURE 11: Comparison of geometry for optimization and final design.



FIGURE 12: Manufactured and mounted propeller for EAV-3.

$r/R=0.133-0.2$ ). Figure 12 shows the final modeling for manufacturing and actual propeller fabricated with composite materials. For the accuracy of manufactured geometry of the propeller, an outer mold is made of aluminum with precision machining. Carbon fiber-reinforced plastic is carefully laminated and fabricated on the outer mold. A total eight pieces of propeller were produced, and quality of product is examined individually.

For an overview, a flow chart which briefly illustrates the design procedure used in the present study is shown in Figure 13.

### 3. Wind Tunnel Test

**3.1. Test Facility and Measurement Device.** The wind tunnel test is conducted to evaluate the performance of the EAV-3 propeller [41, 42]. The test was carried out at KARI low speed wind tunnel with a closed-circuit test section, whose width and height are 4 m and 3 m, respectively. The maximum speed is 120 m/s, and the turbulence intensity is 0.07% at 88 m/s.

A measurement device capable of measuring the performance of propellers having diameters of 1–2 m was designed and installed [41]. Figure 14 shows schematic and modeling of the device. The validity of the measuring concept implemented on the device was confirmed in our previous experimental study conducted for a propeller with a diameter that is less than 1 m by using the same concept [43]. A torque sensor and motor properly arranged behind the propeller constitute the driver module. This module is placed on a pair of cylinder guides, which enable it to freely move back and forth, and connected to a base via a load cell. The force pulling the module forward is directly measured by the load cell as thrust. The torque exerted on the driving shaft is directly measured by the torque sensor between the motor and propeller.

The motor, torque sensor, and load cell were selected based on the prediction of the thrust, torque, and rpm range. To generate the required torque and power output and be capable of precise rpm control, an industrial alternating current motor was used. The motor selected was Mitsubishi's HG-JR 153, with a maximum rpm of 6000, a maximum

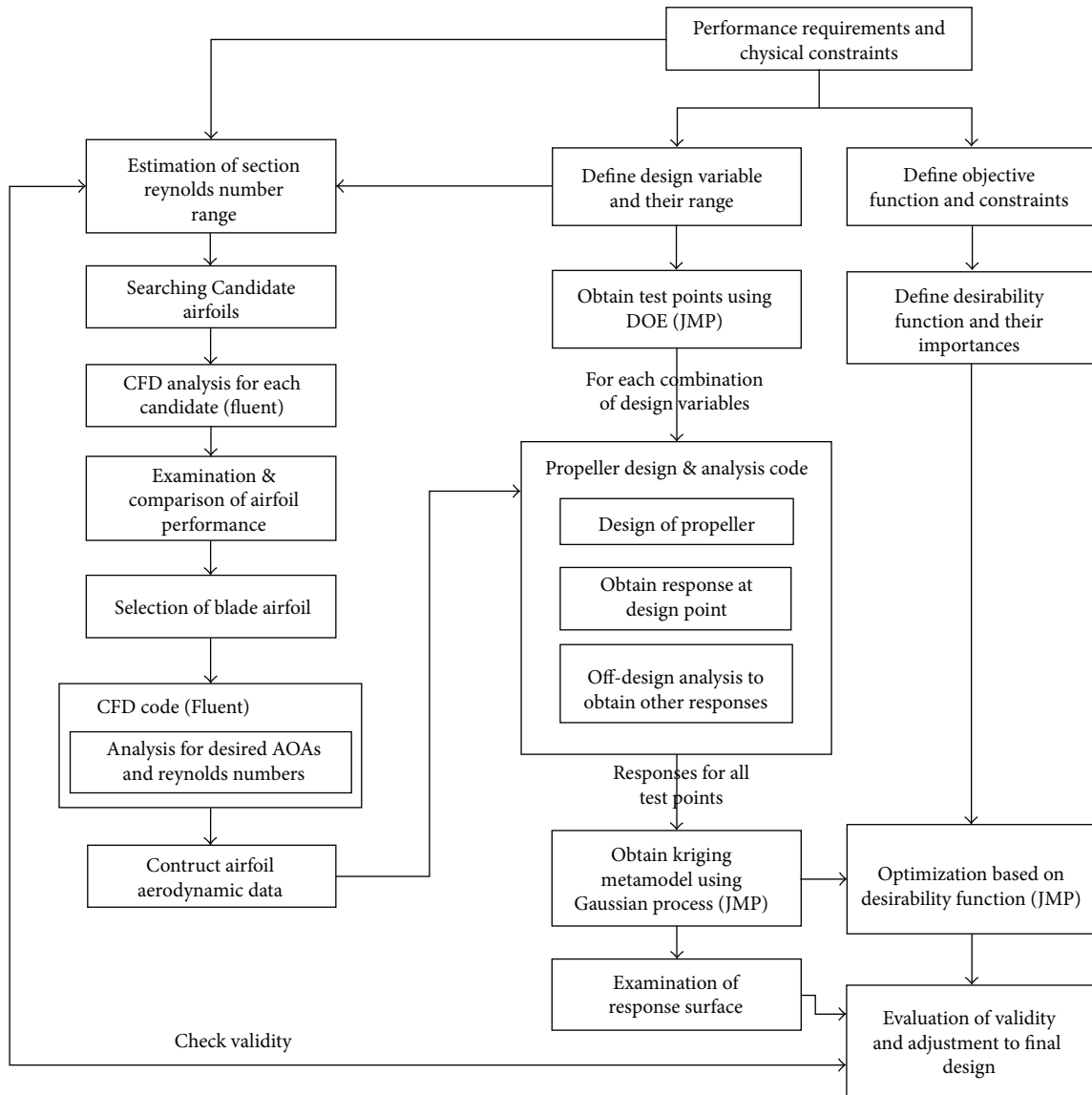


FIGURE 13: Flow chart of design of propeller for EAV-3.

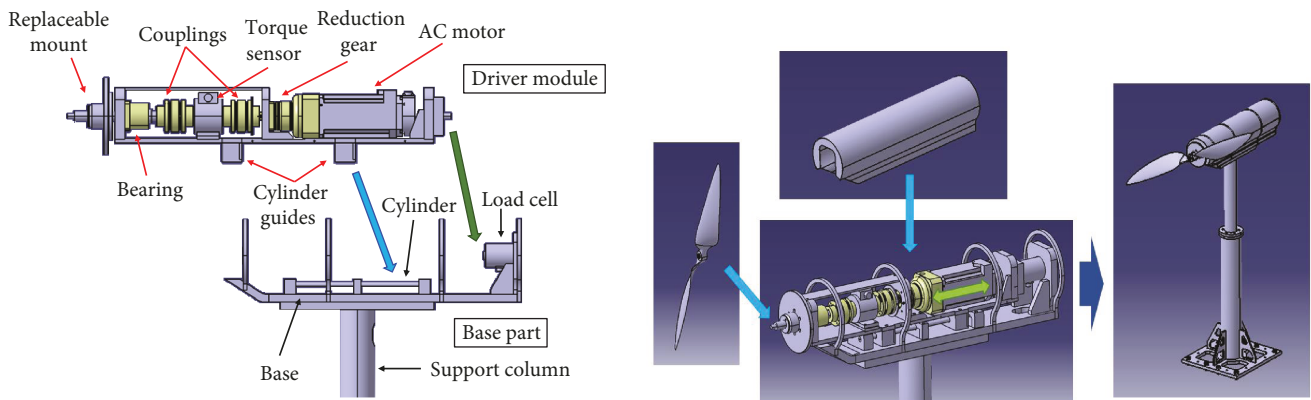


FIGURE 14: Schematic and modeling of measurement device.



FIGURE 15: Installation of measurement device.

torque of 14.3 N·m, and a rated output of 1.5 kW. A reduction gear with a ratio of 3 : 1 was attached to the motor to allow the operation under low rpm and high torque conditions. The load cell and torque sensor chosen were Dacell UMI (20 kgf ) and HBM T-22 (2 kgf·cm), respectively. The rpm is measured using Autonics BF4RP optical sensor with a rotating plate attached to the coupling.

The main structure of the driver module and base is designed as a single part with precision machining to minimize tolerances in the assembly and alignment. The steel use stainless material was used to ensure sufficient strength for minimizing deformation. Starting from the design stage, the assembly method and components carefully considered the alignment accuracy of the rotational axis. The cable connection ports of the torque sensor and motor were modified/remodeled to minimize the outer diameter of the device. The control rack and panel were separately designed and manufactured for the accurate speed control of the motor. Figure 15 shows the manufactured/installed measurement device. The length of the main body is 791 mm, and the outer diameter is 196 mm.

**3.2. Calibration and Data Acquisition.** The sensor calibration was performed using a weight. The load in the direction of the thrust was applied to the load cell in a stepwise manner and thereafter removed. The slope of the obtained signal was then taken as the conversion factor. The load cell signal showed a hysteresis of approximately 0.5~1.0 N, mainly due to the friction force in the cylinder guide. Since the applied torque and signal from the torque sensor are in good agreement with each other, no conversion factor was applied. The first and second zeroes of the sensor were recorded for each run and used as zero offset correction.

The measurement uncertainty of the device was estimated from calibration tests. The errors from both the calibration factor and zero offset correction were estimated to be within 0.1% for both the thrust and torque. Moreover, the same level of errors was confirmed for repeatability and nonlinearity. However, due to the friction in the sliding guide, the hysteresis error for the thrust measurement was relatively high and confirmed as the dominant factor of uncertainty. The total uncertainty in the measured thrust was estimated to be approximately 1.7% at a maximum. As for torque, additional error factors were not identified, and the overall uncertainty was estimated to be within 0.1%. Because the load cell

and torque sensor are independent, and the manufacturing is precisely performed considering the axial alignment, it is considered that the occurrence of the interference error between the sensors and other axes is negligible.

Different from conventional aerodynamic tests, the dynamic pressure is considerably low at 20–50 Pa, because the test of the EAV-3 propeller is usually performed at low wind speeds of less than 10 m/s. In this case, the accurate measurement of the dynamic pressure of freestream is required to ensure reliability and repeatability of results, since the calculated wind speed of the test section will substantially vary according to a small difference in dynamic pressure. The dynamic pressure was determined by measuring the static pressure difference between the stagnation chamber and inlet of the test section. The differential pressure was measured using an MKS Baratron sensor and a Mensor model 2106 transducer. The accuracy is found to be within 1 Pa. The zero values of the differential pressure were recorded in several preliminary tests at various days and times. The data indicated that these zero values change from –3 to 3 Pa, depending on the day and time, even under the wind tunnel stop state. The differential pressures were recorded at the start and end of each run, and the dynamic pressure in the test section was corrected using this value.

The flow temperature was measured with a 100  $\Omega$  resistance temperature detector installed through the side wall of the inlet of the test section. The difference in temperature readings between this detector and another temperature sensor installed in the device was found to be less than approximately 0.2°C. The air density was calculated according to the measured temperature and humidity, and wind speed was calculated from the density and the measured dynamic pressure.

When all sensor signals become stable, data acquired for 5 seconds with sampling rate of 10 Hz were averaged. Thereafter, the thrust and torque of the propeller were determined by applying the corrections.

**3.3. Test Results.** The test was conducted at a fixed rpm and varying wind speed to measure performances at various advance ratios ( $J$ ). Figure 16(a) shows the measured thrust and torque at 700, 867, 950, and 1050 rpm. In the figure, the filled and nonfilled symbols represent the thrust and torque, respectively. Performance coefficients calculated

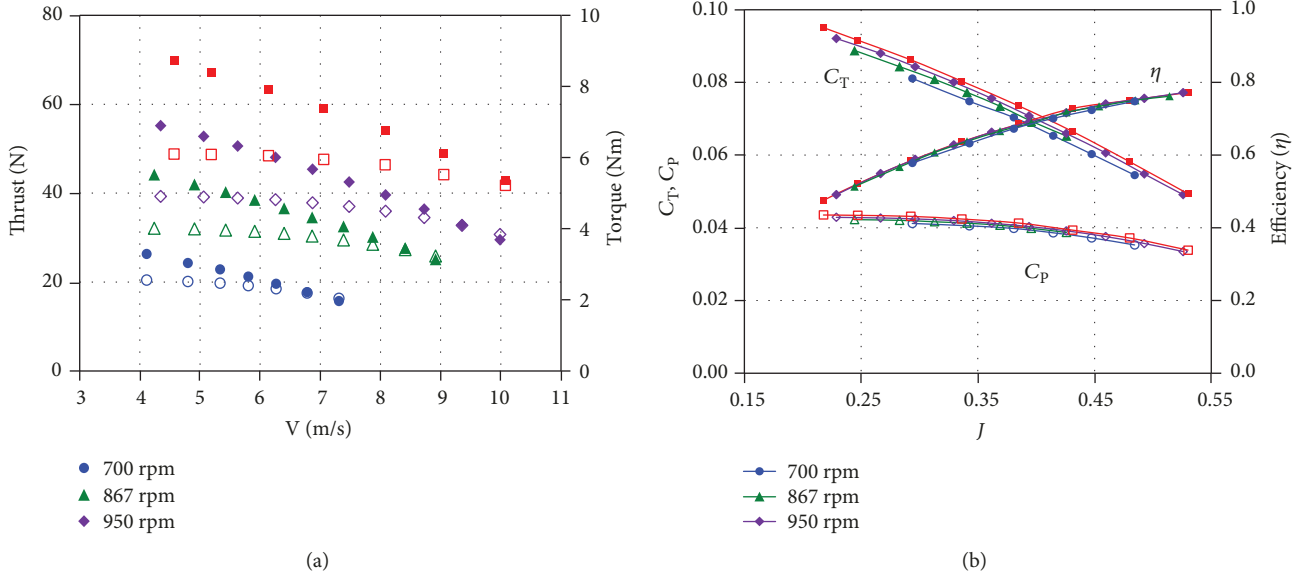


FIGURE 16: (a) Measured thrust and torque and (b) performance coefficients.

from measured data are shown in Figure 16(b). The thrust coefficient ( $C_T$ ), power coefficient ( $C_p$ ), and efficiency ( $\eta$ ) are as defined in (1).

$$\begin{aligned}
 J &= \frac{V}{nD}, \\
 C_T &= \frac{T}{\rho n^2 D^4}, \\
 C_p &= \frac{Q\omega}{\rho n^3 D^5}, \\
 \eta &= J \frac{C_T}{C_p}.
 \end{aligned} \tag{1}$$

The difference among the performance coefficients is observed according to the rpm; the higher the rpm is, the higher the thrust and power coefficients are. The efficiency was practically the same at more than 867 rpm, but slightly lower by approximately 1%p at 700 rpm. In our previous study, it was confirmed that efficiency degradation may occur if the blade chord Reynolds number decreases below  $10^5$  [43]. Similar observations were made in other studies that measured propeller performance in the low Reynolds number range [44, 45]. Considering the rotational speed and chord length of the blade, the condition of 700 rpm ( $Re_c = 10^5 - 2 \times 10^5$ ) is expected to effect a slight decrease in efficiency. However, it is estimated that a considerable decrease in efficiency is further expected at lower rpms.

**3.4. Correction of Wall Blockage Effect.** Even if the propeller generates thrust in the closed test section, the continuity equation at any cross-sectional area of the test section must be satisfied. This yields the same effect as the propeller was under a lower wind speed when it operates in the absence of the wall. As a result, the propeller attains the thrust increasing effect. Glauert correction [46] is commonly used

as a method for correcting the blockage effect [45, 46]. As shown in (2), this method predicts the equivalent freestream velocity ( $V'$ ) for the case without the wall, which yields the same thrust generated in the wind tunnel.

$$\begin{aligned}
 V' &= V \left( 1 - \frac{\tau_4 \alpha_1}{2\sqrt{1+2\tau_4}} \right), \\
 \tau_4 &= \frac{T}{\rho A_{\text{disk}} V^2}, \\
 \alpha_1 &= \frac{A_{\text{disk}}}{A_{\text{tunnel}}}.
 \end{aligned} \tag{2}$$

In addition, various correction techniques have been studied and proposed. However, in order to apply recent methods, the static pressure distribution on the test section wall in the downstream direction must be measured separately [47]. Glauert correction is also known to provide a similar accuracy to the methods that use static pressure measurements in the general advance ration range ( $J = 0.2-0.6$ ) [47].

Figure 17 shows the results of the case of 867 rpm with Glauert correction. For comparison, data without correction are shown as symbols with no fill. As mentioned above, the correction yields a lower freestream speed than the measured wind speed in the test. It can be observed that the performance coefficient curve slightly shifts to the left, and the change in the advance ratio is approximately 0.005–0.01. The results of the two 867 rpm test cases are plotted together in Figure 17. It can be confirmed that the measurement system has good repeatability. It is noted here that the possibility of a change in the performance curve by the wall effect needs to be taken into consideration when the test is conducted in the closed test section. If the influence is not negligible, the test result can be improved by applying the blockage effect correction.

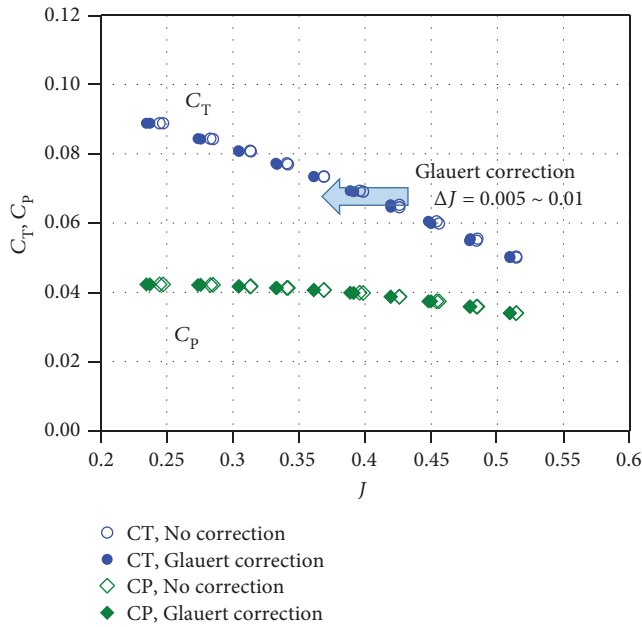


FIGURE 17: Change of performance coefficient due to Glauert correction.

#### 4. CFD Analysis

To evaluate the performance of the propeller, numerical analyses were performed by using a commercial CFD code. It was intended to compare the calculation results with the test data to mutually confirm the reliability and validity of the methods of the wind tunnel test and numerical analysis. The basic approach and method of analysis are the same as that in our previous study on a 0.7 m diameter propeller [43].

**4.1. Computational Grid.** The computational grids are generated by using GAMBIT and T-GRID [46]. For the surface mesh, the blade is composed of structured-type quadrilateral cells. The hub, blade tips, and connecting regions consist of unstructured triangular cells. The total number of surface mesh is approximately  $3 \times 10^5$ . To properly capture the viscous boundary layer on the surface, 18 layers of boundary layer cells are generated with an initial height of  $4 \times 10^{-5}$  m. The height of the first cell from the surface corresponds to a  $y^+$  value of approximately 1.

Figure 18 shows the size of the computational domain and types of boundary conditions. The far boundary is cylindrical in shape. The diameter and height were set to 10 and 15 times the diameter of the propeller, respectively. The inlet and outlet boundaries are located at distances of 5D upstream and 10D downstream, respectively. The velocity inlet boundary condition is imposed at the inlet and side boundaries, whereas the pressure outlet boundary condition is imposed at the outlet boundary.

The region around the propeller is designated as a cylindrical-shaped region, and the boundary between the inside and outside regions is set as an interface. This mesh configuration enables the use of both the multiple reference frame (MRF), which adds a source term to simulate the rotation, and the sliding mesh model (SMM), which directly

rotates the inside region. In the vicinity of the propeller, an unstructured grid of tetrahedral cells was generated at a growth rate of 1.2. The structured-type grid with hexahedron cells are generated for the outer region by dividing it into several blocks. The total number of volume cells is approximately 14.2 million.

**4.2. Method of Analysis.** The commercial CFD code FLUENT [48] was used for the analysis. Since the expected blade tip Mach number which is estimated based on the velocity and rpm did not exceed 0.2, the pressure-based solver was used assuming an incompressible flow. The semi-implicit method for pressure-linked equation (SIMPLE) algorithm was selected for the pressure-velocity coupling. For spatial discretization, the standard method was chosen for pressure, and second-order upwind schemes were used for the other variables. A four-equation model, transition-SST, which is based on  $\gamma$ - $Re_\theta$ , is used as turbulence model. The turbulence intensity at the far boundary and intermittency were set to 0.1% and 0.2, respectively.

In order to reduce the computational cost, the rotation of the propeller is simulated by steady-state calculation of the MRF method. On the other hand, unsteady analysis using the SMM method was individually performed to evaluate the validity of the MRF method. The thrust and torque from the two methods only showed a difference of less than 0.1%. The iteration was continued until the residuals of the continuity equation and other equations were reduced below  $10^{-3}$  and  $10^{-5}$ , respectively, while the thrust and torque were kept constant.

**4.3. Analysis Results.** The test calculation is carried out for the condition of the design point (15 km, 1820 rpm,  $V = 14.6$  m/s). The results are summarized in Table 6 for comparison with prediction from the design code. The design code result is the same with the “final design” result given in Table 5. We note here that the design code result considered only blades without adjustment of the twist angle near the spinner (Section 2.7). On the other hand, the geometry for CFD analyses included the hub, connecting region, and the adjustment of twist angle in the transition region near the spinner. Despite the difference in the geometry, it is evident that the two results are in good agreement. It must be noted that at the design point, the stall is minimized over the entire area of the blade, and the flow at each cross section in CFD becomes practically identical to that of BEMT prediction. Additionally, since the aerodynamic coefficients for BEMT were obtained by the same CFD analysis, we can definitely expect that the CFD results and design code predictions approximate each other.

For an altitude of 15 km and at sea level, analyses at various rpms with a fixed flight speed are conducted. The performance coefficient results with respect to the advance ratio are shown in Figure 19. As previously observed in Table 6, Figure 19(a) shows that, at an altitude of 15 km (design point), the design code predictions and the CFD results agree well, both qualitatively and quantitatively. However, under sea level condition, which corresponds to the off-design point, the design code predictions showed that,

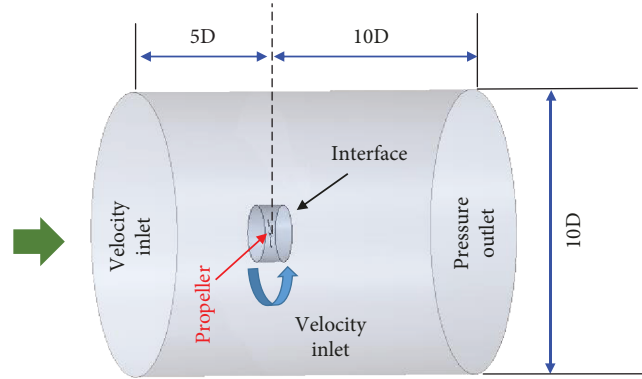


FIGURE 18: Computational domain and boundary conditions for the case of the propeller alone.

TABLE 6: Comparison of performance at design point.

	Thrust (N)	Torque (Nm)	Efficiency (%)
Design code	21.31	2.47	66.0
CFD	21.17	2.48	65.4

to a moderate extent, the thrust coefficient has higher values than those of the CFD, although their tendency agrees well. It is concluded that the design code yields a more optimistic prediction in thrust due to the limitation of BEMT, which does not properly reflect the effect of wake and its contraction at high load conditions.

Figure 19(b) shows the results for cases under various forward speed conditions at 867 rpm. For comparison, the wind tunnel test results of the previous section are shown together with them. The results agree well with test data qualitatively, but the thrust and power coefficients are found to be slightly lower than that of test data. In order to analyze the cause of this difference, the level of uncertainty that can inherently arise from the CFD was evaluated. From grid tests and analyses using other CFD codes, such as OpenFOAM [49] and Star-CCM+ [50], the uncertainties that can arise from CFD are found to be significantly lower than the difference observed in Figure 19(b) [51].

In the wind tunnel test, the measurement devices and support column located downstream of the propeller can cause a blockage effect. Thus, their influence can be considered as one of the causes in the difference between the analysis results and those of the test. Since the results in Figure 19 correspond to cases of propeller-alone analysis, the blockage effect and its level of influence on the wind tunnel test were evaluated.

For convenience and to reduce the number of grids, the geometry of the device and support column are simplified, as shown in Figure 20. The connection between the propeller and device is ignored from the analysis. Approximately 112000 surface meshes and 16 layers of boundary layer cells were generated over the device and column geometry. As depicted in Figure 20(b), the interface surface of cylindrical shape surrounding the propeller was set to separate the inside and outside regions. Different from the case of the propeller alone analysis, the flow symmetry with respect to the rotational axis is not guaranteed in the presence of the device. Therefore, the unsteady analysis with the SMM

technique was performed to directly rotate the propeller in the calculation.

Analyses for several forward speeds with a fixed rpm of 867 were performed. For each case, a total of 12 rotations were calculated with a time step size corresponding to  $2^\circ$  of rotation. The steady solution with the MRF method was obtained first and thereafter used as the initial condition for the unsteady calculation. Figure 21 illustrates the time history of the thrust and torque for several cases. It is observed that the thrust and torque fluctuate with period, which coincides with that of rotation. For the purpose of comparison, the analysis result of the propeller alone case at 5.8 m/s is plotted together with the dashed line. We readily observe that the thrust and torque slightly increase due to the presence of the device and support column.

The thrust and torque were determined as time-averaged values during the last two rotations of the calculation. The summarized results in Tables 7 and 8 are compared with that of the propeller alone analysis. The thrust increased by approximately 1.8–8.9%, and the torque increased by approximately 1.8–7.5%. The level of increase becomes higher as the speed increases (higher advance ratio). The results, including the blockage effect, are shown in Figure 22 together with those in Figure 19. It can be confirmed that the thrust and torque, including the blockage effect, are considerably close to the wind tunnel test data (Figure 22(a)). It is confirmed that the blockage effect has no significant influence on the efficiency (Figure 22(b)) since it increases both thrust and torque. The analysis results show the efficiency to be approximately 1–1.5% higher than that from the wind tunnel data and that their tendency agrees well.

The results imply that the level of the blockage effect from the device and support column should be evaluated properly when constructing a propeller test system. By taking into account the blockage effect in analyzing and processing measured data, accuracy can be improved. In the previous studies on propeller testing [44], the blockage effect was corrected by using the method proposed by Barlow et al. [52]. However, the measured thrust and torque can vary considerably depending on the shape and position of the device. Therefore, it is necessary to evaluate the accuracy of the correction method for each system.

Figure 23 shows the efficiency curves obtained on the basis of the propeller alone analysis under sea level, 15 km,

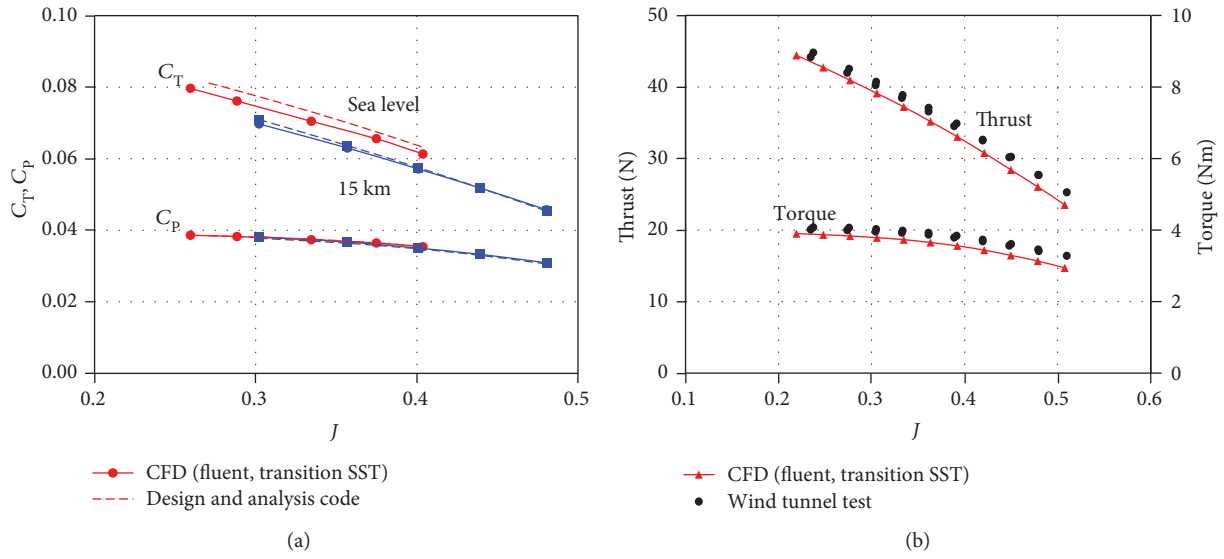


FIGURE 19: Comparison of CFD results with (a) design code and (b) wind tunnel test.



FIGURE 20: Comparison of CFD results with (a) design code and (b) wind tunnel test.

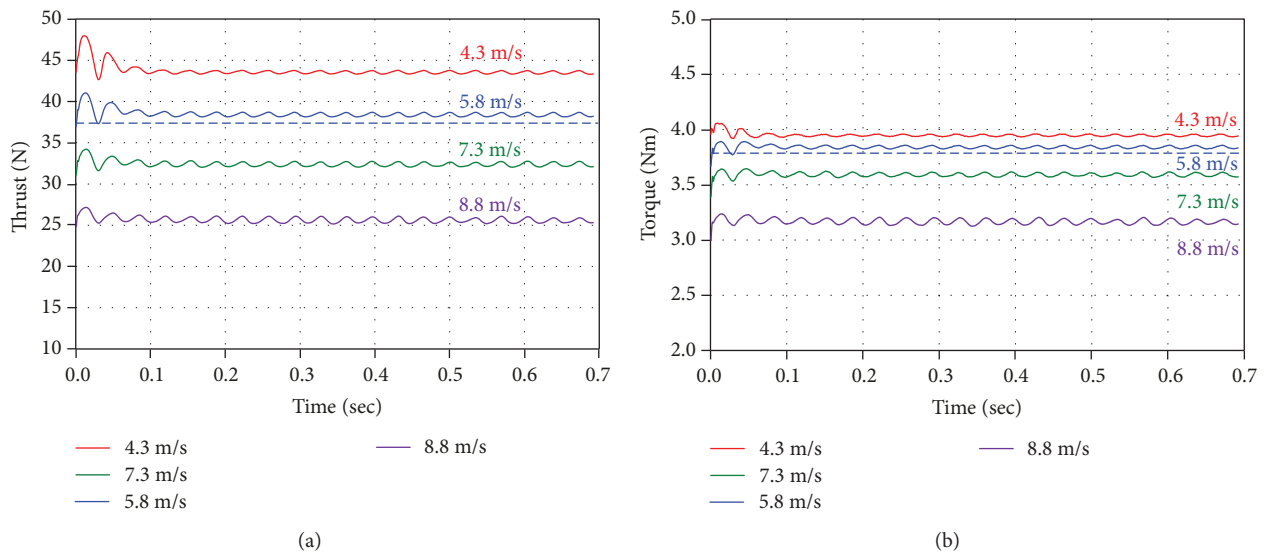


FIGURE 21: Comparison of CFD results with (a) design code and (b) wind tunnel test.

TABLE 7: Comparison of thrust.

V (m/s)	Propeller only	With device/column	Difference
4.3	42.72	43.52	+0.80
5.8	37.22	38.38	+1.16
7.3	30.78	32.38	+1.60
8.8	23.54	25.57	+2.03

TABLE 8: Comparison of torque.

V (m/s)	Propeller only	With device/column	Difference
4.3	3.87	3.94	+0.07
5.8	3.73	3.84	+0.11
7.3	3.44	3.59	+0.15
8.8	2.94	3.16	+0.22

and 18 km altitude conditions. Numerical results clearly show that under high-altitude conditions, the efficiency decreases over the entire range of the advance ratio due to the decrease in the Reynolds number. The reduction in the thrust coefficient and efficiency in the low Reynolds number range have been well known from previous studies on small propellers [44, 45, 53]. However, the design operating advance ratio of EAV-3 increases as the altitude increases. The advance ratios for the sea level, 15 km, and 18 km flights are estimated as  $J = 0.334, 0.401, \text{ and } 0.411$ , respectively. In spite of the reduction in efficiency, it can be observed from Figure 23 that the efficiency of the designed propeller remains at more than 65% even at high altitudes.

## 5. Flight Test Data

In 2015 and 2016, KARI conducted a flight test of EAV-3. The takeoff and flyover of EAV-3 at a low altitude are shown in Figure 24. During the flight, data from various sensors were recorded at 10 Hz in an onboard storage. After landing, these data were collected for analysis. This section intends to briefly discuss the attempt to evaluate the performance of the propeller based on available data and several assumptions.

In the wind tunnel test, propeller performances were directly measured through the sensors. In case of the CFD, the performance was directly obtained through the analysis result. However, in the flight test, the aerodynamic performance of both the propeller and aircraft cannot be measured directly. In order to evaluate the propeller performance accurately, reliable aerodynamic data of the aircraft during its flight are needed and vice versa.

Additionally, during the actual flight, there are practically no steady-state conditions in which parameters, such as speed and attitude, are kept constant. The limitation on the flyable airspace imposed by the government (10 km radius) makes the acquisition of steady-state data considerably difficult since the aircraft must continuously change direction to remain in the airspace. These factors make flight data analysis difficult. Because the aerodynamic performance can be predicted based only on indirect data acquired from

sensors, the uncertainty and prediction error can significantly increase due to the underlying assumptions.

**5.1. Method of Analysis.** The atmospheric density, flight speed, rpm, and thrust and torque values are required to obtain the performance coefficient with respect to the advance ratio. However, all quantities except rpm, which is measured from the rpm sensor, are not directly measured in the flight test but should be estimated from available data. In this study, we attempted to estimate these values according to simple assumptions and approximations.

There are two kinds of altitudes obtainable from the flight data. These are the pressure altitude, which is calculated from the atmospheric pressure measured by the air data system (ADS), and the recorded GPS altitude. The difference between these two altitudes was confirmed to be less than 15 m for the entire flight. The density is assumed to be the standard atmospheric value according to the GPS altitude data. The flight speed is computed using the dynamic pressure measured from ADS and the estimated density. The rpm of each motor was determined by averaging sensor data at 1-second intervals at a particular time of interest. The rpm for data analysis was obtained as average rpm value of the two motors.

The power consumption of the propeller was calculated by using the recorded voltage and current data supplied to the motor electronic speed controller (ESC). The actual power delivered to the propeller was estimated by assuming an ESC efficiency as 96%. The torque is calculated using the rpm and the estimated power. The climb speed (rate of climb in m/s) was determined by average climb speed for 2 s centered at a particular time of interest using the GPS altitude.

To estimate the drag of EAV-3, the drag polar of the main wing was obtained by CFD analysis under several altitude conditions. The basic principle and method of analysis are the same as those described in Section 4. Although the main wing is a flexible structure, it is assumed as rigid body in the analysis. The results are curve fitted to obtain the polynomial equation for the drag coefficient with respect to the angle of attack. The increment in the drag with altitude, which is different for each angle of attack, is assumed to be a quadratic variation, from the sea level to the 18 km analysis results. Based on further analyses, the additional drag by the tail wing and fuselage was approximated to 130 counts at sea level. The degree of the additional drag increase with altitude is assumed to be the same as that of the main wing. The summation of contributions from the main wing and the other parts results in the estimation of the total drag coefficient of EAV-3. The total drag was calculated by multiplying the drag coefficient, dynamic pressure, and wing area.

The power required during the climb flight is calculated by using the drag ( $D$ ), flight speed ( $V$ ), weight ( $W$ ), and climb speed ( $V_c$ ), as given in (3). The propeller thrust is simply predicted from the relationship  $P = TV$  by assuming that the propeller generates the required power.

$$P = DV + WV_c. \quad (3)$$

As mentioned above, it is difficult to maintain a steady state with a fixed attitude due to the continuous maneuvering

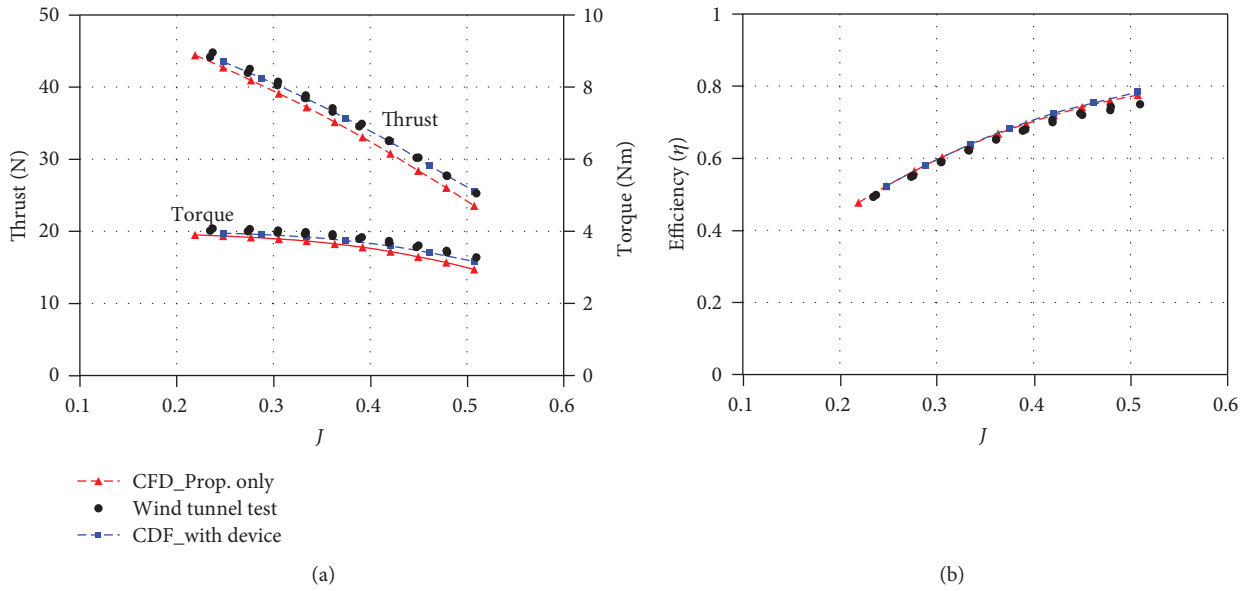


FIGURE 22: Comparison of CFD results with (a) design code and (b) wind tunnel test.

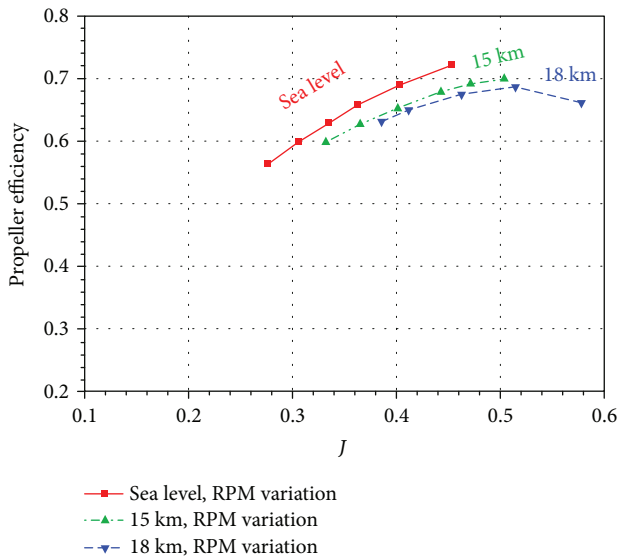


FIGURE 23: Efficiency curves at several altitude conditions.

to remain in the allowable airspace, as well as maintain a desired flight under disturbances of the atmosphere. As an example, Figure 25 depicts several flight data for a duration of 2 min during a climb from an altitude of approximately 3400–3900 m. During this period, the equivalent airspeed and angle of attack fluctuate continuously. Moreover, it is observed that the aircraft performed two major turn maneuvers during the time shown in the figure.

To take into account the approximately steady and stable state to the extent possible, data during the turn maneuver were excluded from the analysis of the propeller performance. For this purpose, only data corresponding to the moments of the roll angle from  $-0.015$  to  $0.015$  rad, roll rate from  $-0.006$  to  $0.006$  rad/s, and yaw rate from  $-0.01$  to  $0.01$  rad/s were considered. For altitudes below 17 km, additional restrictions are imposed on deflection angles of control

surfaces. Data are filtered based on the deflection angles of  $-2$  to  $2^\circ$  and  $-3$  to  $3^\circ$  for the aileron and rudder, respectively. Since EAV-3 adapts rpm differential control, the data on the rpm difference of less than 20 are filtered and chosen for the analysis.

5.2. Results of Analysis. Figure 26(a) shows the time history of two altitudes obtained during the climb of up to 18.5 km. As previously mentioned, the two altitudes are practically identical. It is observed that it took approximately 7.5 hours after takeoff to reach the 18 km altitude. The climb speed with respect to altitude is plotted in Figure 26(b) based on the filtered data. In general, during the flight, the climb speed varied from 0.5 to 1.0 m/s. For convenience, the time region was divided into four sections, designated as A–D in the figure.

The predicted thrust coefficient with respect to the advance ratio at each moment of filtered data is shown in Figure 27. The results corresponding to the four sections are illustrated by symbols with different colors. For the purpose of comparison, CFD results of the propeller alone analysis at several altitudes and wind tunnel test data are plotted together. It can be observed that the estimated values from the flight data are scattered over a wide range around the wind tunnel and CFD data. It is difficult to make a strict quantitative comparison because the degree of dispersion is large.

Nevertheless, several meaningful qualitative tendencies and characteristics can be observed from the comparison. It is evident that the values at lower altitudes (section A) are distributed around the wind tunnel test data and exhibit similar tendencies. It can be conjectured that the flight data contain the blockage effect of the main wing similar to that of the support column in the wind tunnel test. This can be regarded as a possible explanation on the observation that flight data values are slightly higher than CFD results of the propeller alone analysis at sea level.



FIGURE 24: Flight test of EAV-3.

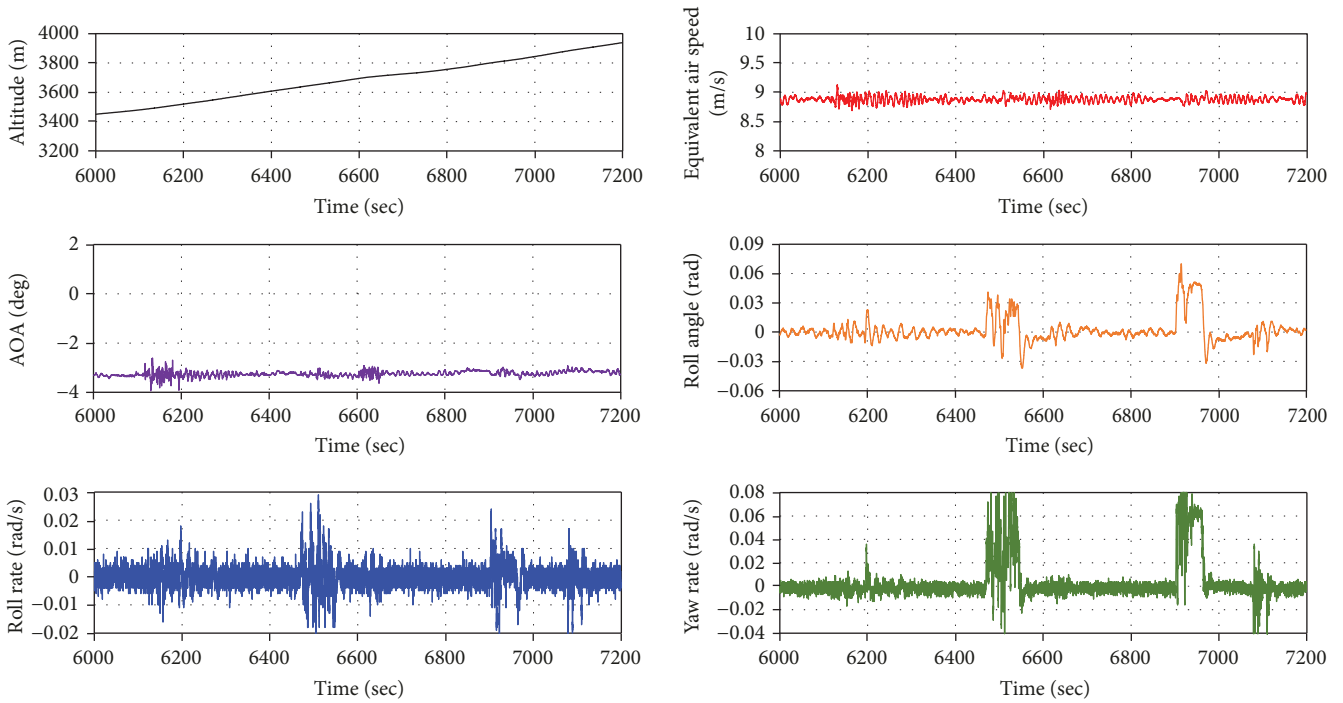
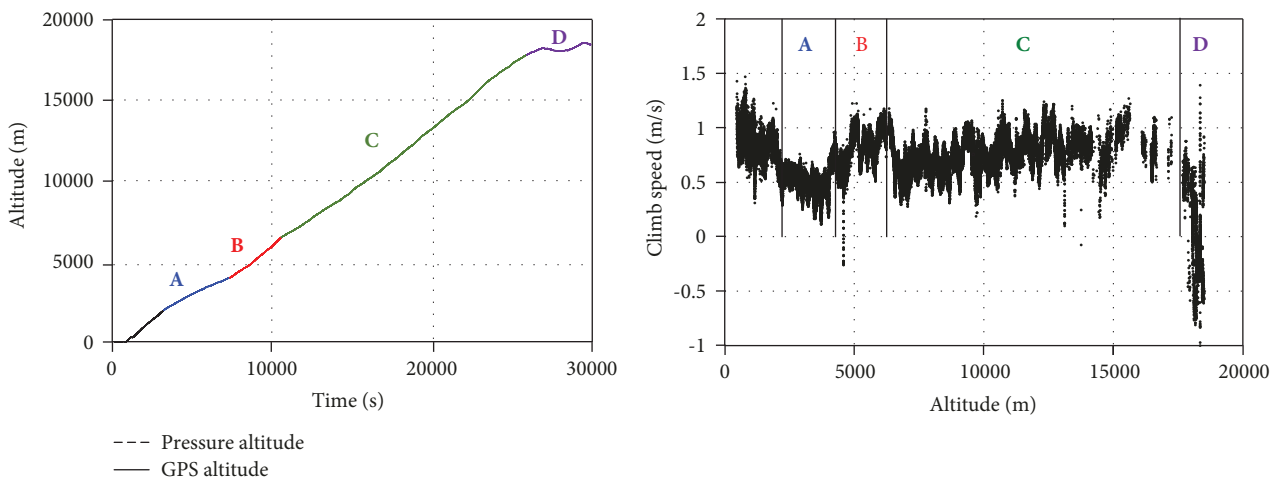


FIGURE 25: Example of flight data (altitude, equivalent air speed, attitude angle, and rate).



(a)

(b)

FIGURE 26: (a) Time history of altitude and (b) climb speed.

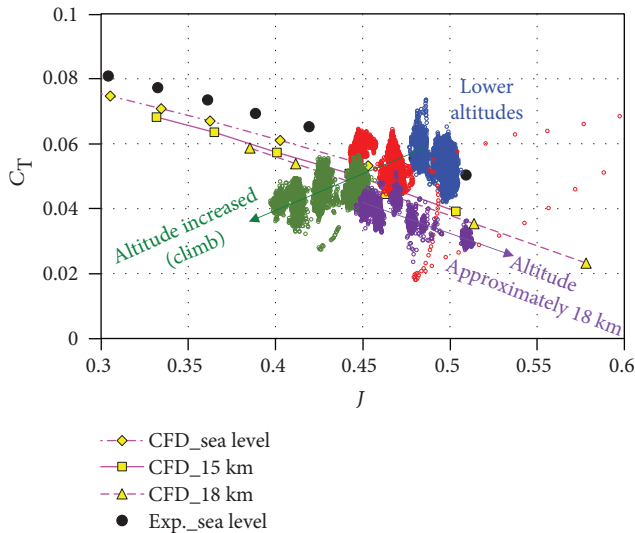


FIGURE 27: Comparison of thrust coefficient results.

The operating advance ratios during climb are in the range of approximately 0.4 to 0.5 and gradually decrease as the altitude increases. This means that the rpm increase was greater than the increase in the flight speed as the altitude increases. It is a different behavior compared with what was expected in the propeller design stage. We note here that the weight of EAV-3 was increased by approximately 10% from its original design after the finalization of its fabrication. Moreover, the final performance of the motor was also enhanced by over 10% in torque compared to that given as constraint of the propeller design. Therefore, it was expected that the propeller was operated under an off-design condition at some extent in the flight test. The flight control algorithm, which is optimized not only for the propeller design philosophy, is also regarded as a reason for the unexpected behavior.

It is evident from the figure that the thrust coefficient considerably decreases as the altitude increases (as changing from A to B, and B to C). This tendency is consistent with CFD prediction and is interpreted as the low Reynolds number effect, which was also confirmed in wind tunnel tests. In section D, which is approximately 18 km in altitude, the propeller operated under various flight conditions, including climb and cruising, resulting in a wide range of operating rpms. Thus, the thrust coefficient is distributed over a wide range of advance ratios for significantly limited altitudes, as shown in the figure. It can be seen that the distribution follows well the tendency of the curve of CFD results from the propeller alone analysis at 18 km. It must be emphasized that the thrust coefficient further decreases to even lower values than that from CFD results. This implies that the degree of decrement that occurred in the actual flight is considerably greater than that in the prediction of CFD using the transition SST model. It must be mentioned here that the evaluation of the thrust coefficient is directly affected by the drag estimation and it can be shifted up and down in the figure depending on the assumptions and approximations.

Figure 28 shows the comparison of results on efficiency. Although the prediction from flight data exhibits a high level

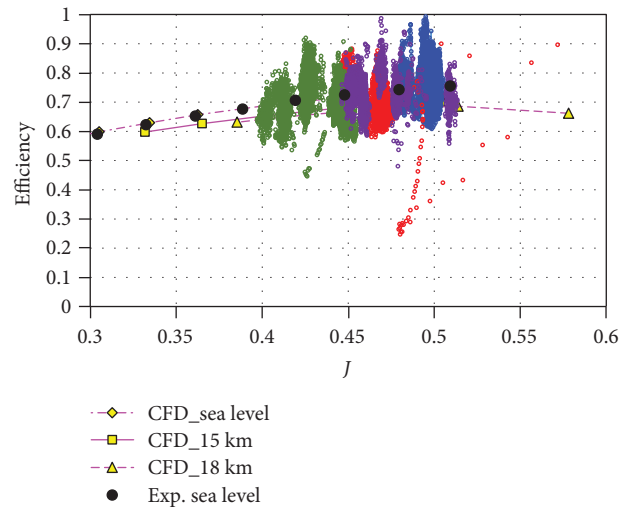


FIGURE 28: Comparison of thrust coefficient results.

of scattering, it is distributed around the wind tunnel test and CFD results and follows well their tendencies along a wide range of advance ratios. However, it is noted that the flight data seem slightly shifted to higher values. It is suspected that this optimistic prediction is primarily due to the inaccuracy arises from the estimation of power consumption. Since the estimation is simply based on voltage and current data, it is anticipated that a relatively large uncertainty would be introduced. Apparently, a more reliable strategy to obtain the power consumption would be necessary to improve accuracy. On the other hand, it is observed that the propeller operated in the advance ratio ranges, where the maximum efficiency is expected from the wind tunnel test and CFD data. This implies that the fundamental objective of the propeller design is successfully achieved.

## 6. Conclusion

In this paper, the design and performance evaluation of the propeller of KARI's HALE UAV were introduced.

For the design, a basic methodology was established based on BEMT and minimum induced loss. The aerodynamic data of the airfoil were constructed by using CFD to ensure the reliability under low Reynolds number conditions. The blade airfoil was chosen based on the evaluation of the lift-to-drag ratio for expected Reynolds numbers under the design condition. The effect of the design lift coefficient distribution on high-altitude conditions was investigated, and the characteristics of low Reynolds number behavior were analyzed. Design variables and responses for the design were selected, and the response surface was examined based on DOE and kriging metamodel. After defining the objective function and constraints, the optimization was conducted based on the desirability function. The final design was determined from the examination of the optimization result.

The wind tunnel test and numerical analysis were conducted to evaluate the performance of the propeller and validity of the design. The measurement device was designed, constructed, and calibrated. The method of data acquisition

and correction was established. The performance of the designed propeller was measured under several conditions. The changes in performance as the low Reynolds number decreases were confirmed from the test data. The numerical analysis was conducted by using a commercial CFD code, and the results showed that the tendency was in good agreement with the test data. However, the thrust and torque are slightly lower than those in the test. The analyses, including the device and support column in the wind tunnel test, were further carried out to confirm that the thrust and torque were increased. It was found that the results approximated the test data, and the experimental and numerical results showed good agreement. It can be inferred from the comparison that the blockage effect must be appropriately considered to either interpret or correct measured data.

Flight test data are analyzed to evaluate the performance of the propeller in an actual flight. Due to inherent limitations in the flight test data, several assumptions and approximations were made to obtain the variables required to calculate performance. Approximately 8 h of data during the climb of up to 18 km altitude were analyzed. In spite of dispersion of analyzed data, the results for the thrust coefficient and efficiency generally exhibited good agreement in their tendencies, and satisfactory agreement in their quantitative comparison. The degradation of the thrust coefficient as the altitude increased was clearly observed in the flight data. Moreover, the level of decrease with respect to the altitude was found to be greater than the prediction obtained from CFD analysis. It was confirmed that the propeller operated over the advance ratio ranges, where the maximum efficiency is expected from both wind tunnel test and CFD analysis. This implies that the design methodology used in this study is practically useful and valid for the development of high-altitude propellers.

## Data Availability

The data used to support the findings of this study are available from the corresponding author upon request.

## Conflicts of Interest

The authors declare that there is no conflict of interest regarding the publication of this paper.

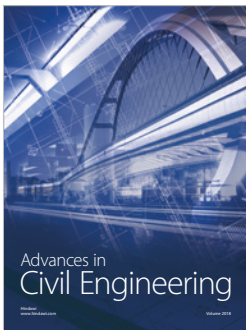
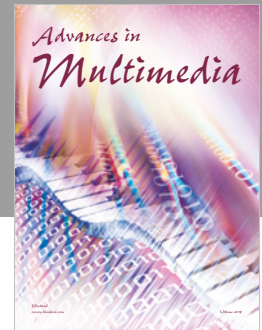
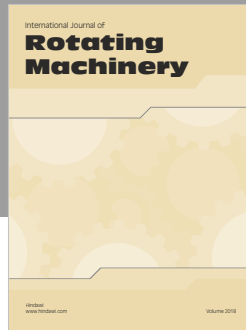
## Acknowledgments

This work was supported by the National Research Foundation of Korea (NRF) grant funded by the Korea government (MSIP) (no. 2017R1C1B1010109) and Pusan National University Research Grant, 2016.

## References

- [1] G. Romeo, G. Frulla, E. Cestino, and G. Corsino, "HELIPLAT: design, aerodynamic, structural analysis of long-endurance solar-powered stratospheric platform," *Journal of Aircraft*, vol. 41, no. 6, pp. 1505–1520, 2004.
- [2] C. L. Nickol, M. D. Guynn, L. L. Kohout, and T. A. Ozoroski, "High altitude long endurance air vehicle analysis of alternatives and technology requirements development," in *45th AIAA Aerospace Sciences Meeting and Exhibit*, pp. 1–17, Reno, NV, USA, 2007, AIAA 2007-1050.
- [3] B. S. de Mattos, N. R. Secco, and E. F. Salles, "Optimal design of a high-altitude solar-powered unmanned airplane," *Journal of Aerospace Technology and Management*, vol. 5, no. 3, pp. 349–361, 2013.
- [4] L. Sai, Z. Wei, and W. Xueren, "The development status and key technologies of solar powered unmanned air vehicle," *IOP Conference Series: Materials Science and Engineering*, vol. 187, article 012011, 2017.
- [5] L. J. Ehernberger, C. Donohue, and E. H. Teets, "A review of solar-powered aircraft flight activity at the Pacific missile range test facility, Kauai, Hawaii," in *11th AMS Conference on Aviation, Range, and Aerospace Meteorology*, pp. 1–7, Hyannis, MA, USA, 2004.
- [6] [https://en.wikipedia.org/wiki/Helios\\_Prototype](https://en.wikipedia.org/wiki/Helios_Prototype).
- [7] <https://www.airbus.com/defence/uav/zephyr.html>.
- [8] A. Rapinett, *Zephyr: a high altitude long endurance unmanned air vehicle*, [M.S. thesis], University of Surrey, 2009.
- [9] [https://en.wikipedia.org/wiki/Boeing\\_SolarEagle](https://en.wikipedia.org/wiki/Boeing_SolarEagle).
- [10] Y. Lee, S. Hwang, S. Kim, C. Kim, S. Ahn, and D. Lee, "Development of an electrically powered HALE UAV," in *Proceeding of the 2013 KSAS Spring Conference*, vol. 1, pp. 1097–1100, Jeongseon, Korea, 2013.
- [11] Y. Lee, S. Hwang, S. Kim et al., "Development and flight tests of a scaled electrically powered HALE UAV," in *Proceeding of the 2014 KSAS Fall Conference*, pp. 797–800, Jeju, Korea, 2014.
- [12] Y. Lee, S. Hwang, S. Kim, and S. Kim, "Development of a full-scale solar powered HALE UAV," in *Proceeding of the 2015 KSAS Fall Conference*, pp. 181–184, Jeju, Korea, 2015.
- [13] S. Hwang, S. Kim, Y. Lee, and C. Kim, "Design of the solar powered high altitude long endurance (HALE) unmanned aerial vehicle," in *Proceeding of the 2015 KSAS Fall Conference*, pp. 950–954, Jeju, Korea, 2015.
- [14] S. J. Hwang, S. G. Kim, C. W. Kim, and Y. G. Lee, "Aerodynamic design of the solar-powered high altitude long endurance (HALE) unmanned aerial vehicle (UAV)," *International Journal of Aeronautical and Space Sciences*, vol. 17, no. 1, pp. 132–138, 2016.
- [15] A. Colozza, *High Altitude Propeller Design and Analysis Overview*, Federal Data Systems, Cleveland, OH, USA, 1998.
- [16] J. S. Monk, *A Propeller Design and Analysis Capability Evaluation for High Altitude Application*, [M.S. Thesis], University of the Witwatersrand, 2010.
- [17] H. Glauert, "Airplane propellers," in *Aerodynamic Theory*, W. F. Durand, Ed., pp. 169–360, Springer, Berlin, Heidelberg, 1935.
- [18] <http://web.mit.edu/drela/Public/web/qprop/>.
- [19] M. A. R. Silvestre, J. Morgado, and J. C. Pascoa, "JBLADE: a propeller design and analysis code," in *2013 International Powered Lift Conference*, pp. 1–12, Los Angeles, CA, USA, 2013, AIAA 2013-4220.
- [20] M. H. McCrink and J. W. Gregory, "Blade element momentum modeling of low-Re small UAS electric propulsion systems," in *33rd AIAA Applied Aerodynamics Conference*, pp. 1–23, Dallas, TX, USA, 2015, AIAA 2015-3296.
- [21] M. K. Rwigema, *The Evaluation of a Low-Order Propeller Performance and Wake Prediction Capability for the Calculation of Power Effects*, [M.S. thesis], University of the Witwatersrand, 2014.

- [22] <https://sites.google.com/site/joamorgado23/downloads>.
- [23] <http://www.mh-aerotoools.de/airfoils/javaprop.htm>.
- [24] C. N. Adkins and R. H. Liebeck, "Design of optimum propellers," *Journal of Propulsion and Power*, vol. 10, no. 5, pp. 676–682, 1994.
- [25] D. Park and C. Kim, "Development of HALE propeller design and analysis program," in *Proceedings of KSAS 2014 Fall Conference*, pp. 1039–1042, Jeju, Korea, 2014.
- [26] M. Drela, "XFOIL: an analysis and design system for low Reynolds number airfoils," in *Low Reynolds Number Aerodynamics*, T. J. Mueller, Ed., pp. 1–12, Springer, Berlin, Heidelberg, 1989.
- [27] <http://www.xflr5.com/xflr5.htm>.
- [28] <https://www.ansys.com/Products/Fluids/ANSYS-Fluent>.
- [29] F. R. Menter, R. B. Langtry, S. R. Likki, Y. B. Suzen, P. G. Huang, and S. Völker, "A correlation-based transition model using local variables: part I — model formulation," in *ASME Turbo Expo 2004: Power for Land, Sea, and Air*, pp. 57–67, Vienna, Austria, June 2004, ASME GT2004-53452.
- [30] R. J. McGhee, B. S. Walker, and B. F. Millard, "Experimental results for the Eppler 387 airfoil at low Reynolds numbers in the Langley low-turbulence pressure tunnel," Tech. Rep. NASA-TM-4062, NASA, 1988.
- [31] M. S. Selig and B. D. McGranahan, "Wind tunnel aerodynamic tests of six airfoils for use on small wind turbines," in *42nd AIAA Aerospace Sciences Meeting and Exhibit*, pp. 1–19, Reno, NV, USA, 2004, AIAA 2004-1188.
- [32] H. Hu and Z. Yang, "An experimental study of the laminar flow separation on a low-Reynolds-number airfoil," *Journal of Fluids Engineering*, vol. 130, no. 5, article 051101, 2008.
- [33] L. W. Traub and E. Cooper, "Experimental investigation of pressure measurement and airfoil characteristics at low Reynolds numbers," *Journal of Aircraft*, vol. 45, no. 4, pp. 1322–1333, 2008.
- [34] M. Sahin, J. Hall, K. Mohseni, and K. Hillewaert, "Direct numerical simulation of separated low-Reynolds number flows around an Eppler 387 airfoil," in *46th AIAA Aerospace Sciences Meeting and Exhibit*, pp. 1–21, Reno, NV, USA, 2008, AIAA 2008-422.
- [35] J. Morgado, M. A. R. Silvestre, and J. C. Páscoa, "Full range airfoil Polars for propeller blade element momentum analysis," in *2013 International Powered Lift Conference*, pp. 1–10, Los Angeles, CA, USA, 2013, AIAA 2013-4379.
- [36] J. Dorfling and K. Rokhsaz, "Integration of airfoil stall and compressibility models into a propeller blade element model," *Journal of Aerospace Engineering*, vol. 29, no. 4, article 04016014, 2016.
- [37] D. C. Montgomery, *Design and Analysis of Experiments*, John Wiley & Sons, Inc., 6th edition, 2005.
- [38] G. G. Wang, "Adaptive response surface method using inherited Latin hypercube design points," *Journal of Mechanical Design*, vol. 125, no. 2, pp. 210–220, 2003.
- [39] J. P. C. Kleijnen, "Kriging metamodeling in simulation: a review," *European Journal of Operational Research*, vol. 192, no. 3, pp. 707–716, 2009.
- [40] [https://www.jmp.com/en\\_us/home.html](https://www.jmp.com/en_us/home.html).
- [41] T. Cho, D. Park, S. Lee, Y. Kim, and Y. Lee, "Development of wind tunnel test system for solar-powered HALE UAV Propeller," in *Proceeding of the 2015 KSAS Spring Conference*, Jeongseon, Korea, 2015.
- [42] C. Teahwan, K. Yangwon, and P. Donghun, "Wind tunnel test for the propeller performance of the high altitude UAV," *Journal of the Korean Society for Aeronautical & Space Sciences*, vol. 46, no. 3, pp. 189–196, 2018.
- [43] D. Park, T. Cho, C. Kim, Y. Kim, and Y. Lee, "Performance evaluation of propeller for high altitude by using experiment and computational analysis," *Journal of the Korean Society for Aeronautical & Space Sciences*, vol. 43, no. 12, pp. 1035–1047, 2015.
- [44] J. B. Brandt and M. S. Selig, "Propeller performance data at low Reynolds numbers," in *49th AIAA Aerospace Sciences Meeting including the New Horizons Forum and Aerospace Exposition*, pp. 1–18, Orlando, FL, USA, 2011, AIAA 2011-1255.
- [45] M. A. R. Silvestre, J. Morgado, P. Alves, P. Santos, P. Gamboa, and J. C. Páscoa, "Propeller performance measurement at low Reynolds numbers," *International Journal of Mechanics*, vol. 9, pp. 154–166, 2015.
- [46] H. Glauert, *The Element of Aerofoil and Airscrew Theory*, Cambridge University Press, Second edition, 1948.
- [47] R. E. Fitzgerald, *Wind Tunnel Blockage Corrections for Propellers*, [M.S. Thesis], University of Maryland, 2007.
- [48] Fluent, <https://www.ansys.com>.
- [49] OpenFOAM, <https://www.openfoam.org>.
- [50] STAR-CCM+, <https://mdx.plm.automation.siemens.com/star-ccm-plus>.
- [51] D. H. Park, C. W. Kim, and Y. G. Lee, "Comparison of commercial and open source CFD codes for aerodynamic analysis of flight vehicles at low speeds," *Journal of Computational Fluids Engineering*, vol. 21, no. 2, pp. 70–80, 2016.
- [52] J. B. Barlow, W. H. Rae, and A. Pope, *Low-Speed Wind Tunnel Testing*, John Wiley and Sons, New York, NY, USA, Third edition, 1999.
- [53] M. P. Merchant, *Propeller Performance Measurement for Low Reynolds Number Unmanned Aerial Vehicle Applications*, [M.S. Thesis], Wichita State University, 2004.



**Hindawi**

Submit your manuscripts at  
[www.hindawi.com](http://www.hindawi.com)

